

Mesozoic Crustal Thickening of the Longmenshan Belt (NE Tibet, China) by Imbrication of Basement Slices: Insights From Structural Analysis, Petrofabric and Magnetic Fabric Studies, and Gravity Modeling

Zhenhua Xue, Guillaume Martelet, Wei Lin, Michel Faure, Yan Chen, Wei Wei, Shuangjian Li, Qingchen Wang

▶ **To cite this version:**

Zhenhua Xue, Guillaume Martelet, Wei Lin, Michel Faure, Yan Chen, et al.. Mesozoic Crustal Thickening of the Longmenshan Belt (NE Tibet, China) by Imbrication of Basement Slices: Insights From Structural Analysis, Petrofabric and Magnetic Fabric Studies, and Gravity Modeling. Tectonics, 2017, 36 (12), pp.3110-3134. 10.1002/2017TC004754 . insu-01707791

HAL Id: insu-01707791
https://insu.hal.science/insu-01707791

Submitted on 13 Feb 2018

HAL is a multi-disciplinary open access archive for the deposit and dissemination of scientific research documents, whether they are published or not. The documents may come from teaching and research institutions in France or abroad, or from public or private research centers.

L'archive ouverte pluridisciplinaire **HAL**, est destinée au dépôt et à la diffusion de documents scientifiques de niveau recherche, publiés ou non, émanant des établissements d'enseignement et de recherche français ou étrangers, des laboratoires publics ou privés.

AGU PUBLICATIONS

Tectonics

RESEARCH ARTICLE
10.1002/2017TC004754

Key Points:
- Contemporaneous NW shearing and SE thrusting facilitate the extrusion of the basement slices
- Two parallel belts of basement slices imbricated southeastward constitute the bulk architecture of the Longmenshan thrust belt and adjacent areas
- The imbricated basement slices have already thickened the crust of the Longmenshan area in Mesozoic times

Supporting Information:
- Supporting Information S1

Correspondence to:
W. Lin,
linwei@mail.iggcas.ac.cn

Citation:
Xue, Z., Martelet, G., Lin, W., Faure, M., Chen, Y., Wei, W., … Wang, Q. (2017). Mesozoic crustal thickening of the Longmenshan belt (NE Tibet, China) by imbrication of basement slices: Insights from structural analysis, petrofabric and magnetic fabric studies, and gravity modeling. *Tectonics*, *36*, 3110–3134. https://doi.org/10.1002/2017TC004754

Received 4 AUG 2017
Accepted 8 NOV 2017
Accepted article online 20 NOV 2017
Published online 18 DEC 2017

©2017. American Geophysical Union. All Rights Reserved.

Mesozoic Crustal Thickening of the Longmenshan Belt (NE Tibet, China) by Imbrication of Basement Slices: Insights From Structural Analysis, Petrofabric and Magnetic Fabric Studies, and Gravity Modeling

Zhenhua Xue[1,2,3], Guillaume Martelet[4], Wei Lin[1], Michel Faure[3], Yan Chen[3], Wei Wei[1], Shuangjian Li[5], and Qingchen Wang[1]

[1]State Key Laboratory of Lithospheric Evolution, Institute of Geology and Geophysics, Chinese Academy of Sciences, Beijing, China, [2]Institutions of Earth Sciences, University of Chinese Academy of Sciences, Beijing, China, [3]Institut des Sciences de la Terre d'Orléans, Université d'Orléans, UMR 7327, CNRS/INSU, Orléans, France, [4]Bureau de Recherche Géologique et Minière UMR 7327, Orléans, France, [5]Institute of Petroleum Exploration and Development, China Petroleum and Chemical Corporation, Beijing, China

Abstract This work first presents field structural analysis, anisotropy of magnetic susceptibility (AMS) measurements, and kinematic and microstructural studies on the Neoproterozoic Pengguan complex located in the middle segment of the Longmenshan thrust belt (LMTB), NE Tibet. These investigations indicate that the Pengguan complex is a heterogeneous unit with a ductilely deformed NW domain and an undeformed SE domain, rather than a single homogeneous body as previously thought. The NW part of the Pengguan complex is constrained by top-to-the-NW shearing along its NW boundary and top-to-the-SE shearing along its SE boundary, where it imbricates and overrides the SE domain. Two orogen-perpendicular gravity models not only support the imbricated shape of the Pengguan complex but also reveal an imbrication of high-density material hidden below the Paleozoic rocks on the west of the LMTB. Regionally, this suggests a basement-slice-imbricated structure that developed along the margin of the Yangtze Block, as shown by the regional gravity anomaly map, together with the published nearby seismic profile and the distribution of orogen-parallel Neoproterozoic complexes. Integrating the previously published ages of the NW normal faulting and of the SE directed thrusting, the locally fast exhumation rate, and the lithological characteristics of the sediments in the LMTB front, we interpret the basement-slice-imbricated structure as the result of southeastward thrusting of the basement slices during the Late Jurassic-Early Cretaceous. This architecture makes a significant contribution to the crustal thickening of the LMTB during the Mesozoic, and therefore, the Cenozoic thickening of the Longmenshan belt might be less important than often suggested.

1. Introduction

At the northeastern margin of the Tibetan Plateau, the Longmenshan belt is remarkable for its steep topographic gradient with a thickened crust of approximately 60 km as well as the intensive seismic activity, such as the devastating M_w 8.0 Wenchuan (2008) and M_w 7.0 Lushan (2013) earthquakes (Figure 1a) (Guo et al., 2013). Numerous investigations have been carried out to study the formation of the thickened crust and elevated topography (Hubbard & Shaw, 2009; Royden et al., 2008; Tapponnier et al., 2001; Yin & Harrison, 2000).

The Longmenshan thrust belt (LMTB) is a composite orogen that records multiphase southeastward thrusting during the Mesozoic and Cenozoic (Bureau of Geology and Mineral Resources of Sichuan Province (BGMRSP), 1991; Burchfiel et al., 1995; Chen et al., 1995) and a period of top-to-the-NW shearing (Burchfiel et al., 1995; Tian et al., 2016 ; Xu et al., 2008). The widespread top-to-the-SE shearing has been interpreted as the consequence of the Mesozoic continental collision between the North China Block and South China Block (SCB) overprinted by Cenozoic continental collision between the India and Eurasia Blocks (Burchfiel et al., 1995; Xu et al., 2008). The top-to-the-NW shearing mostly developed associated with the orogen-parallel Neoproterozoic complexes (Tian et al., 2016; Xu et al., 2008); yet both of the NW shearing and the complexes remain controversial in terms of mechanism, scale, and timing (Burchfiel et al., 1995; Tian et al., 2016; Xu et al., 2008; Zhou et al., 2008). On the basis of extent and timing of the top-to-the-NW shearing and the

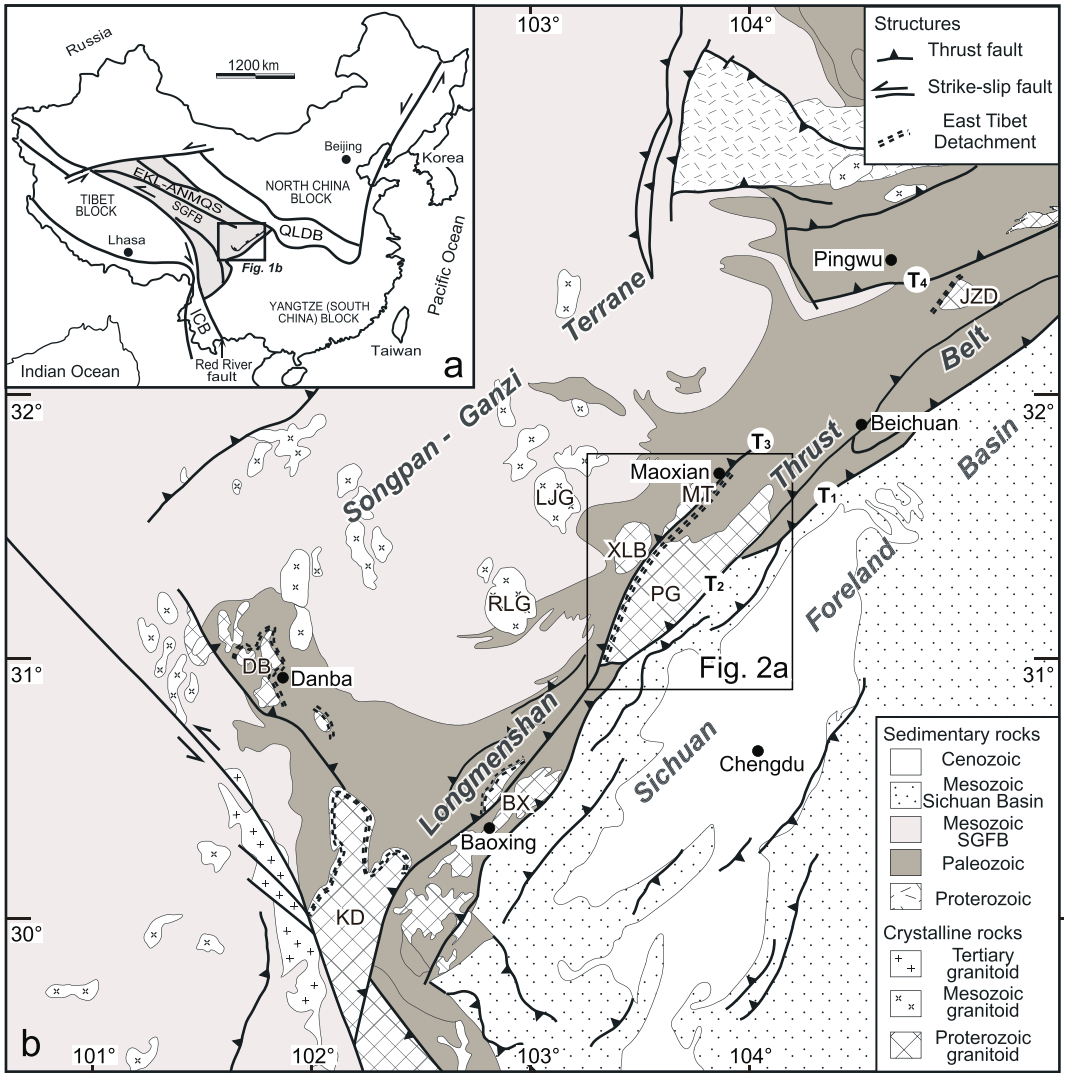


Figure 1. (a) Simplified tectonic sketch of China. QL: Qingling-Dabie orogenic belt; EKL-ANMQS: East Kunlun-A'nyemaqen suture; SGT: Songpan-Ganzi terrane; LMTB: Longmenshan thrust belt; and ICB: Indochina Block; (b) Simplified geological map of the Longmenshan thrust belt, modified after BGMRSP (1991), Burchfiel et al. (1995), and Xu et al. (2007). T_1: Anxian-Guanxian Fault (AGF); T_2: Yingxiu-Beichuan Fault (YBF); T_3: Wenchuan-Maowen Fault (WMF); T_4: Qingchuan Fault (QCF); JZD: Jiaoziding complex; PG: Pengguan complex; XLB: Xuelongbao complex; BX: Baoxing complex; KD: Kangding complex; DB: Danba dome; RLG: Rilonguan granite; LJG: Laojungou granite; and MT: Moutuo complex.

emplacement of the Neoproterozoic complexes, several models have been proposed: (i) Cenozoic lower crustal channel flow bounded by NW and SE directed shear zones, buttressed to the SE by the old and strong lithosphere of the Sichuan basin that sustains the high topography of the Longmenshan (Burchfiel et al., 2008; Royden et al., 2008); (ii) crustal shortening by thrust faults that formed duplex structure of the LMTB (Hubbard & Shaw, 2009; Tapponnier et al., 2001; Tian et al., 2016); and (iii) the extrusion of a crustal wedge during the Cretaceous (Xu et al., 2008). The understanding of the top-to-the-NW shearing and the emplacement of the Neoproterozoic complexes therefore is crucial to unravel the evolution of the LMTB as well as the uplifting of the Tibetan Plateau.

The Neoproterozoic Pengguan complex, located in the middle segment of the LMTB, is cored by granitic rocks and deformed by the top-to-the-NW shearing; thus, the Pengguan complex provides an ideal place to unravel the tectonic history of the LMTB (Figure 1b). For this study, we conducted a field-based structural analysis, anisotropy of magnetic susceptibility (AMS) measurements, and microstructural analysis, aiming to constrain the structural geometry and deformation intensity of the Pengguan complex. This is

complemented with gravity modeling of the Pengguan complex and adjacent areas, which provides a high-resolution image of the upper crust structures. Integrating published geochronological data and lithological characteristics of the sediments inside the Sichuan foreland basin to the SE, the new multidisciplinary results from this study provide a comprehensive understanding of the tectonic evolution of the LMTB.

2. Geological Setting

The regional structure of the LMTB is defined by three listric thrust faults that strike northeast and steeply dip to the northwest, namely, from northwest to southeast, the Wenchuan-Maoxian Fault (WMF, T_3 in Figure 1b), the Yingxiu-Beichuan Fault (YBF, T_2 in Figure 1b), and the Anxian-Guanxian Fault (AGF, T_1 in Figure 1b) (Xu et al., 1992). A set of orogen-parallel Neoproterozoic complexes, for example, the Jiaoziding complex, the Pengguan complex, the Xuelongbao complex, the Baoxing complex, the Kangding complex, the Danba dome, are distributed from NE to SW along the LMTB (Figure 1b).

To the NW of the LMTB, the Songpan-Ganzi Terrane (SGT) is characterized by an extensively folded turbidite of Middle-Late Triassic age, more than 7 km in thickness. This folded unit is intruded by tens of syntectonic and posttectonic granites that dominantly derive from the partial melting of the SGT Neoproterozoic basement and a variable proportion of sedimentary rocks as well as negligible amounts of material of mantle source (Figure 1b; Hu et al., 2005; Roger et al., 2004; Zhang et al., 2007, 2006). The Paleozoic-Late Triassic sedimentary cover is separated from the Neoproterozoic basement by a regional décollement and transported southward (Calassou, 1994; Harrowfield & Wilson, 2005). To the east of the LMTB, the Sichuan foreland basin, underlain by a Neoproterozoic basement, records flexural subsidence due to the thrusting of the LMTB (Chen, Wilson, et al., 1994).

In the LMTB, both Early Mesozoic and Cenozoic shortenings have been documented. The Early Mesozoic shortening is the result of transpressional interaction between the SGT and the SCB, which resulted in structural inversion of the western margin of the Yangtze Block from a pre-Middle Triassic rift to a SE verging fold-and-thrust belt. Pervasive southeast/south-southeastward thrusting developed at different scales in (i) the Sichuan foreland basin and (ii) the hinterland on the west of the WMF (Burchfiel et al., 1995; Worley & Wilson, 1996; Xu et al., 1992; Yan et al., 2011). In the foreland basin, the orogen-parallel klippen and nappes were transported southeastward and tectonically overlie on the extensively folded Late Triassic rocks (Figure 2a). Most of the klippen are exposed as synclines overturned to the SE. Southeastward thrusting is also indicated by SE verging folds and locally developed sigmoidal tectonic lenses in the Late Triassic sandstone-mudstone interbeds (Figures 2b and 2e). In the hinterland, macroscopic-scale sigmoidal quartz boudins, asymmetric pressure shadow and microscopic scale of shear bands, mica fishes, and asymmetric plagioclase porphyroclasts on the *XZ* plane (perpendicular to the field observed foliation and parallel to the field observed lineation) indicate an unambiguous top-to-the-SE shearing (Figures 2b and 2c).

The timing of the Mesozoic shortening is first constrained by the unconformity between the Lower Jurassic conglomerates and the intensively folded Upper Triassic sandstone in the Sichuan foreland basin, which indicates a deformation age during T_3-J_1 (BGMRSP, 1991). Second, most plutons intruded in the SGT yield a peak age around 211 Ma that postdates the folding of the SGT and the SE verging folds of the LMTB (BGMRSP, 1991; Hu et al., 2005; Roger et al., 2004; Sigoyer et al., 2014; Xiao et al., 2007; Zhang et al., 2006). Third, $^{39}Ar/^{40}Ar$ dating of metamorphic rocks from the northern segment of the LMTB provides a range of ages between 237 and 208 Ma that were interpreted as minimum timing constraints for this deformation (Yan et al., 2011). Due to southeastward propagation of the LMTB, the Sichuan foreland basin initiated during the Late Triassic with depositional environment changing significantly from shallow marine carbonate platform to terrestrial clastic basin (Chen, Deng, et al., 1994).

The Mesozoic thrust belt and the underlying autochthon were reactivated and thrusted southeastward during the Cenozoic (Figures 1b and 2b). This was interpreted as the response to the northward indentation of India into the Eurasia Block (Burchfiel et al., 2008; Tapponnier et al., 1982; Yan et al., 2011). This brittle, SE directed Cenozoic deformation is expressed by brittle faults with slicken lines, and southeastward overturned Jurassic rocks in the LMTB. Low-temperature geochronology reveals fast exhumation (approximately 90–100 m Myr^{-1}) of the LMTB during the Cenozoic, controlled by the main listric thrusts (Arne et al., 1997; Cook et al., 2013; Enkelmann et al., 2006; Godard et al., 2009; Tian et al., 2013; Wang et al., 2012). The

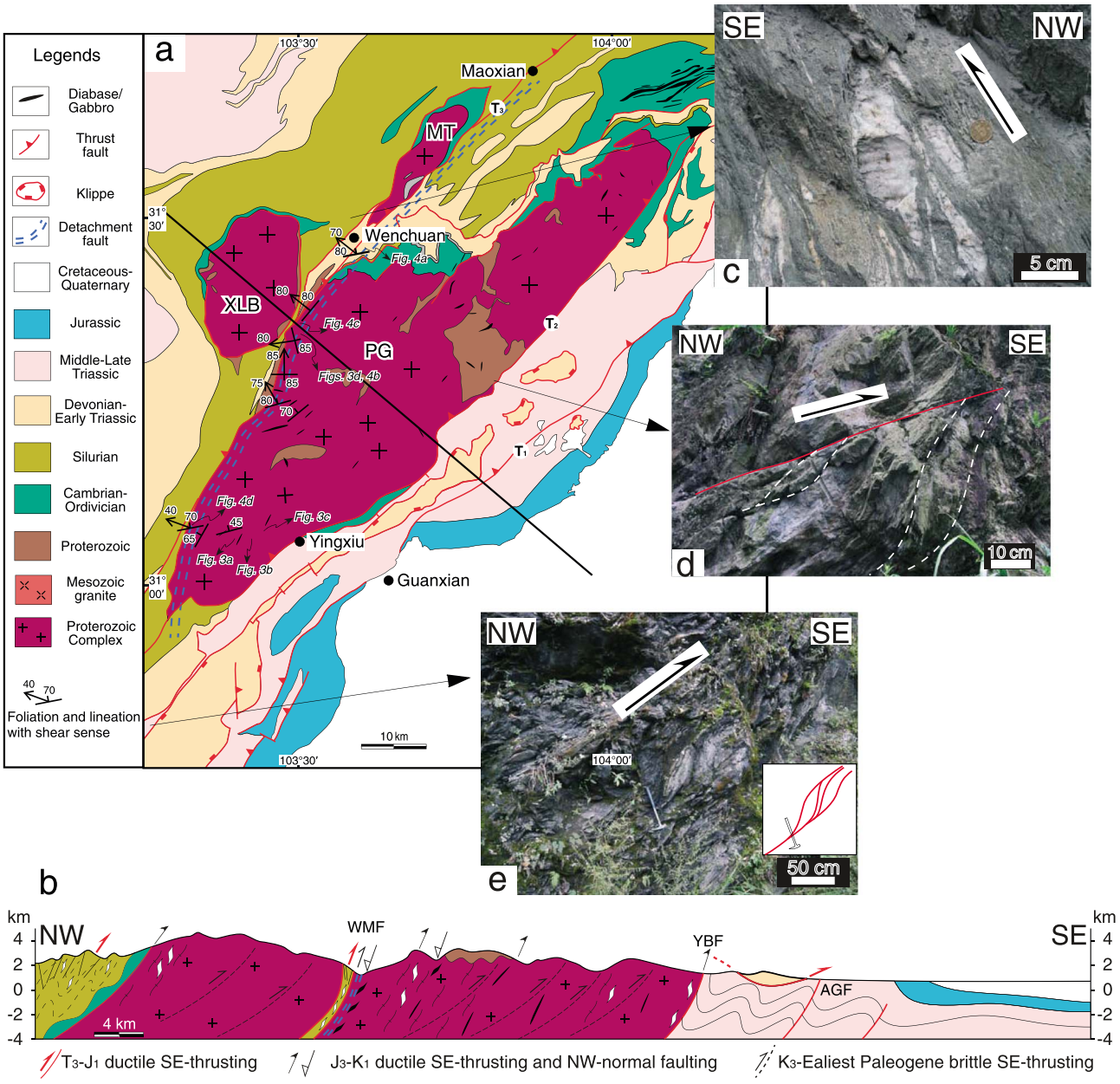


Figure 2. (a) Structural map of the Pengguan complex and adjacent area. (b) Cross-section crossing the Pengguan complex and Xuelongbao complex. (c) Quartz boudin wrapped in the Silurian schist indicates a top-to-the-SE shearing, northwest to the Wenchuan city (31°29.758′N, 103°34.535′E). (d) Shear zone developed in the Proterozoic meta-sandstone display a top-to-the-SE sense of shear, immediately in the hanging wall of the Beichuan-Yingxiu Fault (31°15.62′N, 103°46.96′E). (e) Sigmoidal lens in the Late Triassic sandstone-mudstone interbeds indicates a top-to-the-SE shearing (30°47.843′N, 103°14.615′E). Symbols and acronyms are the same as in Figure 1.

absence of coeval adjacent foreland basin may be due to narrowly distributed and predominantly vertical displacements along the high-angle listric reverse faults in the LMTB (Feng et al., 2015).

Between the Early Mesozoic and Cenozoic shortening, there is an intermediate phase of deformation during the Late Jurassic to Early Cretaceous (Figure 2b). Structural analysis and $^{39}Ar/^{40}Ar$ dating of deformed muscovite reveal a NW-SE directed compressional phase along the belt, on the west of the WMF that resulted in crustal thickening and associated Barrovian-type amphibolite facies metamorphism around 133–120 Ma (Arne et al., 1997; Dirks et al., 1994; Worley et al., 1995). In the Pengguan complex, the top-to-the-SE shearing was dated at 140–135 Ma or circa 166 Ma by $^{39}Ar/^{40}Ar$ dating on the deformed muscovite (Airaghi et al., 2017;

Yan et al., 2008). A belt characterized by top-to-the-NW/N shearing defined as the East Tibet Detachment, mainly developed at the north or NW boundary of the Neoproterozoic complexes that extend from the Danba dome to the middle Longmenshan and may extend to the Jiaoziding complex (Figure 1b) (Xu et al., 2007). It is worth noting that this fault formed at circa 166–120 Ma based on the $^{39}Ar/^{40}Ar$ dating on the deformed micas (Huang, Buick, et al., 2003; Huang, Maas, et al., 2003; Li, 2009; Tian et al., 2016; Xu et al., 2008) and therefore overlaps with the top-to-the-SE tectonics. In the LMTB, both top-to-the-SE and top-to-the-NW shearing were developed with steeply NW dipping foliation and steeply NW plunging lineation (Dirks et al., 1994; Xu et al., 2008). The SGT exhibits low regional cooling rates of approximately 2–3°C/Myr since Late Triassic to Tertiary (Huang, Buick, et al., 2003; Roger et al., 2011), and thus, the deformation during Late Jurassic to Early Cretaceous is more likely restricted to the periphery of the SGT.

In the Sichuan foreland basin, sediments display cyclicity of wedge-shaped and tabular megasequences that indicate three stages of SE motion of the LMTB during (i) Late Triassic-Early Jurassic, (ii) Late Jurassic-Early Cretaceous, and (iii) Late Cretaceous-Eocene (Chen, Wilson, et al., 1994; Li et al., 2013). The episodic sedimentation in the Sichuan foreland basin has been interpreted as the response to the aforementioned three periods of events.

3. Structural Analysis of the Pengguan Complex

3.1. Lithotectonic Units and Bulk Architecture

The NE-SW trending Pengguan complex, bounded by the YBF to the southeast and the WMF to the northwest, is composed of Neoproterozoic granitic rocks and sedimentary rocks of Huangshuihe group (Figure 1b) (BGMRSP, 1991). The granitic rocks are coarse-grained biotite tonalite, fine-grained biotite granodiorite, and two-mica granodiorite, which yield an emplacement age of 809 ± 3 Ma by zircon U-Pb dating (Figure 3a) (Yan et al., 2008). From base to the top, the Huangshuihe group consists of pyroclastic rocks, spilite, crystalline limestones, graphitic schists, sericite quartz schists, and quartzites (BGMRSP, 1991). Lastly, a set of NE-SW trending mafic diabase and gabbro sills intruded the Pengguan complex during 195–186 Ma (Figures 2a and 3c) (Chen et al., 2015). Several NE trending and SE directed thrusts are developed at the NE and SW periphery of the complex (Figure 2a).

Subhorizontal joints represent the main structural pattern of the Pengguan granitic rocks (Figure 3b). Although previous work documented several NE-SW trending shear zones developed inside the complex (Ma et al., 1996), the ductile planar and linear structural elements are not clearly expressed in the field. Even when a planar fabric can be observed in the field, a mineral lineation is not always visible. Only in the NW boundary of the complex, the ductile deformation is clearly characterized by NW dipping foliation and NW plunging lineation (Figure 2a). On its SE margin, the metamorphic rocks of the Huangshuihe group suffered extensive folding and shearing that are consistent with the YBF activity.

3.2. Kinematic Analysis

Macroscopic and mesoscopic structural analysis document two opposite senses of shear in the Pengguan complex, namely, a top-to-the-SE and a top-to-the-NW shearing.

The top-to-the-NW shearing is obvious in the NW boundary of the Pengguan complex, at the footwall of the WMF. This NW dipping fault separates Silurian rocks to the NW from Neoproterozoic rocks to the SE, with a consistent normal component of movement (Figure 2a). The shear foliation dips steeply to the NW, and the lineation plunges steeply to the NW. The rare foliation steeply dipping to the southeast/south probably results from tilting of the original foliation during the Cenozoic deformation (Figure 2a). In thin sections, mica fishes, quartz ribbon aggregates, sigmoidal clasts, and shear bands on *XZ* plane of the sericite-quartz schist and granitic mylonite from the western boundary of the Pengguan complex indicate a consistent top-to-the-NW shearing (Figures 4a–4d). Within the mylonite, the mineral assemblage that defines the foliation and the lineation includes quartz + feldspar + biotite + muscovite + chlorite, suggesting that the shearing was developed under greenschist facies metamorphic conditions (Figure 4). Furthermore, Figure 4b displays subgrain rotation dynamic recrystallizations in quartz indicating the deformation temperature approximately 400–500°C (Parsons, Law, et al., 2016).

In the southeastern boundary of the Pengguan complex, in the hanging wall of the YBF, a top-to-the-SE sense of shear is demonstrated by the extensively folded and cleaved Proterozoic Huangshuihe group, in

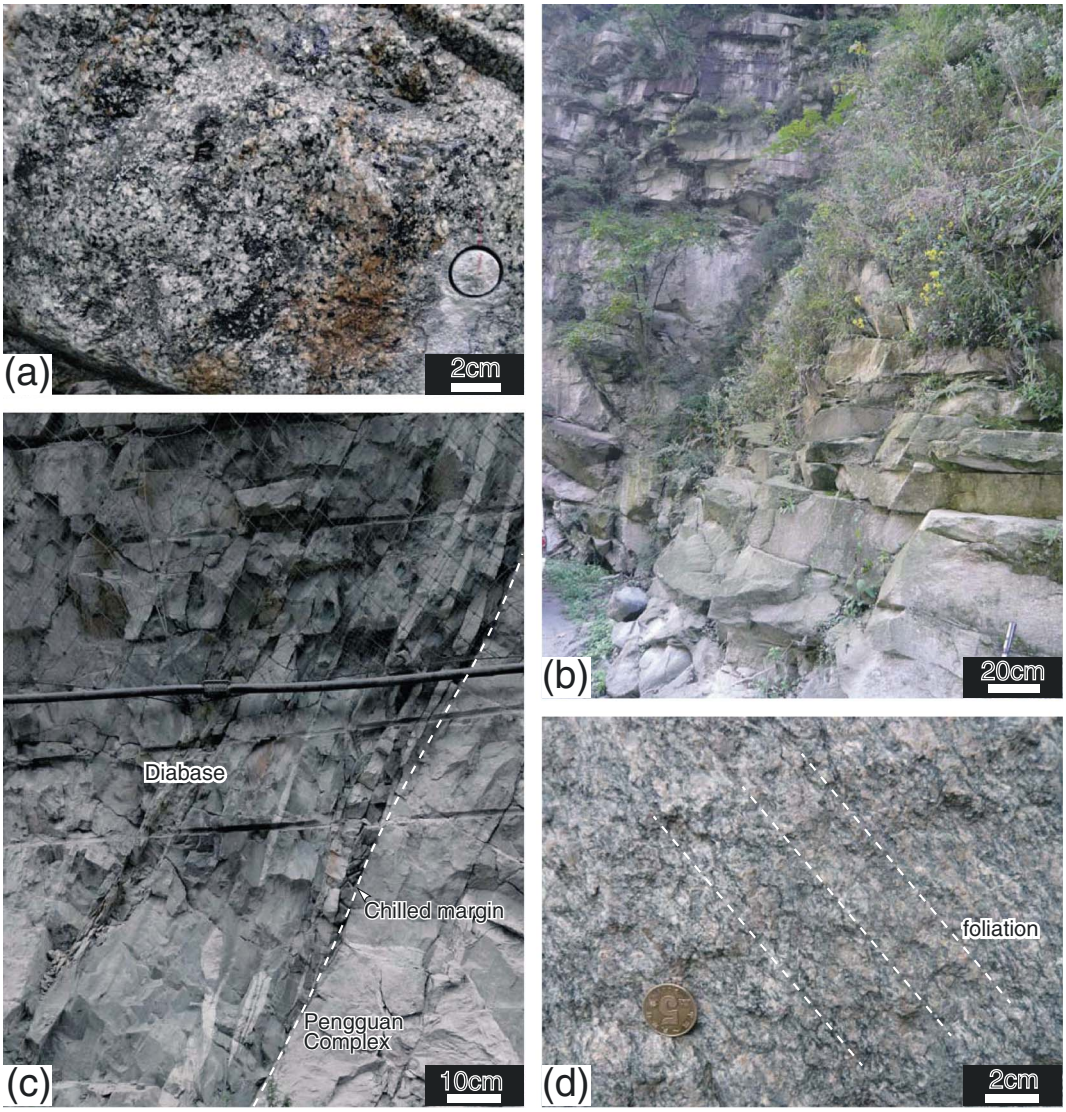


Figure 3. Photographs showing field characters of the Pengguan complex. (a) Undeformed massive diorite (31°3.77′N, 103°23.19′E). (b) Undeformed granodiorite with well-developed subhorizontal joints (31°04.315′N, 103°26.520′E). (c) Diabase dyke intruding the diorite (31°06.66′N, 103°28.88′E). (d) Intensively mylonitized diorite (31°22.931′N, 103°30.364′E). Locations are presented in Figure 2a.

which deflected cleavage roots into a meter-scale SE verging thrust fault (Figure 2d). Compared to the top-to-the-NW shearing, the SE verging shearing in the SE boundary, developed under a low metamorphic grade since no porphyroblasts or other minerals recrystallized there. However, both the top-to-the-SE and top-to-the-NW shearing under greenschist facies metamorphism conditions were distributed in the NW domain of the Pengguan complex as constrained by AMS and petrofabric study in section 4 below.

4. Anisotropy of Magnetic Susceptibility (AMS) and Petrofabric Study

Granitic rocks are often used as a proxy to study regional tectonics due to their ability to record their emplacement setting and their postsolidus deformation (Guineberteau et al., 1987). However, it is difficult to distinguish secondary postsolidus fabrics from primary magmatic ones preserved in granitic rocks merely by field observation, especially when the granite is weakly deformed and/or fine grained (Sen et al., 2014; Wallis et al., 2014). Fortunately, the anisotropy of magnetic susceptibility (AMS) has been proven as an efficient method to reveal the fabrics of granitic rocks (e.g., Borradaile & Henry, 1997; Bouchez, 2000;

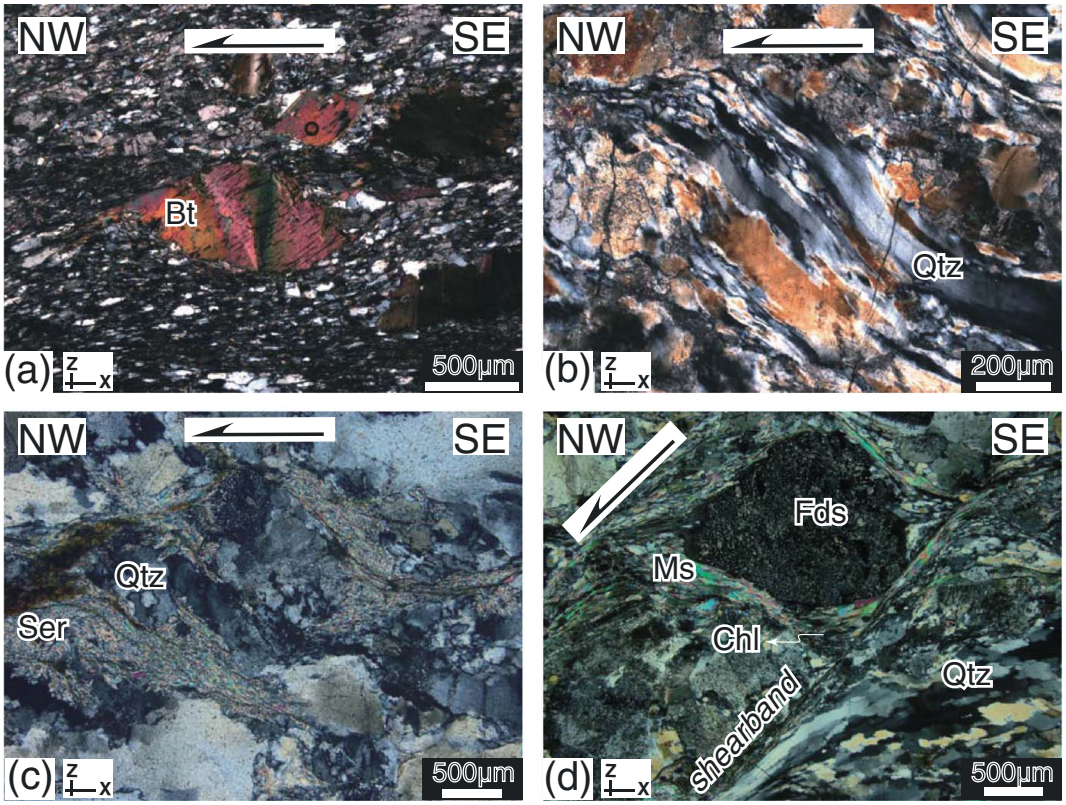


Figure 4. Microscopic features indicate top-to-the-NW shearing in the NW boundary of the Pengguan complex. (a) Mica fish in the Devonian sericite-quartz schist (31°28.445′N, 103°34.479′E). (b) Ribbon quartz aggregates in the granitic mylonite (31°22.444′N, 103°30.551′E). (c) Sericite aggregates wrap quartz porphyroclasts in the granitic mylonite (31°23.39′N, 103°30.99′E). (d) Shear band and sigmoidal porhyroblasts in the granitic mylonite (31°05.193′N, 103°18.730′E). *X* and *Z* axes are marked on the figures. Qtz: quartz, Cal: calcite, Bt: biotite, Ms: muscovite, Ser: sericite, Chl: chlorite, and Fds: feldspar.

Talbot et al., 2005; Wei, Chen, et al., 2014), and a combined microstructural analysis has been applied to the Pengguan granitic rocks in order to decipher its emplacement mechanism and deformation history.

Magnetic susceptibility (*K*) is the ratio of the induced magnetization (*M*) of a specimen to the externally applied magnetic field (*H*) (Borradaile & Jackson, 2004, 2010). The anisotropy of magnetic susceptibility (AMS) is a second rank tensor that describes directional variation of a specimen's magnetic susceptibility, which can be used as deformation proxy if the contributing factors (mineral content, mineral shape fabric, and crystallographic fabric) are determined (Borradaile & Jackson, 2004, 2010; Kruckenberg et al., 2010; Parsons, Ferré, et al., 2016). The AMS is geometrically represented by an ellipsoid defined by three orthogonal principal axes, K_1 (maximum), K_2 (intermediate), and K_3 (minimum) (Tarling & Hrouda, 1993). K_1 and K_3 corresponding to the magnetic lineation and the pole of the magnetic foliation, respectively. The mean magnetic susceptibility (K_m) is computed as $(K_1 + K_2 + K_3)/3$, which represents the sum effect of the magnetic carriers of the specimen.

Three types of magnetic carriers (namely diamagnetic, paramagnetic, and ferromagnetic) have been classified based on their induced magnetization strength and polarity (Tarling & Hrouda, 1993). Induced magnetization of paramagnetic (e.g., phyllosilicate) and ferromagnetic (e.g., magnetite) minerals displays the same polarity as the externally applied field, while the ferromagnetic minerals exhibit much higher susceptibility. Conversely, induced magnetization of diamagnetic (e.g., quartz and calcite) minerals presents the opposite polarity to the external field but with a lower intensity. An important distinction between these three types is that diamagnetic and paramagnetic materials have no magnetic remanence, while the ferromagnetic minerals, such as magnetite, do have a magnetic remanence.

The overall rock magnetic fabric is determined by all magnetic minerals, including but not limited to, their abundance and distribution, the grain shape preferred orientation, the crystallographic preferred orientation, and extent of magnetostatic interaction of ferromagnetic minerals (Borradaile & Jackson, 2004). The grain size

of the ferromagnetic minerals also influences the magnetization by determining the number of magnetic domains (a magnetic domain refers to a zone where a single magnetic pole is displayed). The ferromagnetic grains classified as single domain (SD), pseudo single domain (PSD), and multidomain (MD) based on its grain size varying from smallest to largest (Tarling & Hrouda, 1993). The MD and PSD magnetite display "normal AMS" (the shape of the magnetic ellipsoid resembles the grain shape), while the SD magnetite display "inverse AMS" (Ferré, 2002). Generally, the most abundant, high susceptibility, and strongly anisotropic minerals control the whole-rock AMS fabrics (Borradaile & Jackson, 2004, 2010). Magnetostatic interactions between ferromagnetic grains also influence the AMS that depends on the spatial distribution and concentration of the ferromagnetic grains (Hargraves et al., 1991; Muxworthy et al., 2004; Stephenson, 1994).

The corrected degree of anisotropy describes eccentric extent of the AMS ellipsoid from a sphere ($P_j = 1$) to an ellipsoid ($P_j > 1$) (Jelinek, 1981).

$$Pj = \exp\sqrt{2\sum(\ln Ki - \ln Km)^2}. \quad (1)$$

K_i refers to the three susceptibility axes, K_1, K_2, and K_3. The shape parameter T defines the shape of the magnetic ellipsoid ranging from prolate ($T = -1$) through neutral ($T = 0$) to oblate ($T = +1$) (Jelinek, 1981).

$$T = \frac{\ln(F) - \ln(L)}{\ln(F) + \ln(L)} \text{ where } L = \frac{K1}{K2} \text{ and } F = \frac{K2}{K3}. \quad (2)$$

4.1. Methods of AMS Analysis

A sampling of 299 oriented cores from 36 sites regularly covering the southern Pengguan complex with an interval of 1.5 km has been carried out along the main N-S and W-E trending valleys and several small valleys inside the complex, and also at its periphery (Table 1 and Figure 7). Due to the high topography and access difficulty, the sampling coverage in the northeastern part is relatively low. Approximately six cores about 4 to 6 cm in length and 2.5 cm in diameter and separated by nearly 2 m intervals were collected from each site. Cores were oriented by magnetic compass and, when possible, by solar compass. To avoid the shape effect on the magnetic anisotropy, all cores were cut into 2.2 cm in length to mimic the spherical shape with respect to the 2.5 cm diameter.

Magnetic fabric measurements were performed at the Institute of Geology and Geophysics of Chinese Academy of Sciences. Specimens cut from each sample were analyzed using AGICO Kappabridge (MFK1) magnetic susceptometer operating in low field (300 A/m) to construct the AMS ellipsoid orientation and corresponding magnetic fabric parameters. Measurements include (1) thermomagnetic experiments, (2) isothermal remanent magnetization, and (3) hysteresis properties of small rock fragment on the Micro 3900 Vibrating Sample Magnetometer to determine the magnetic carriers that contributed to the magnetic susceptibility.

4.2. Magnetic Mineralogy

The site magnetic susceptibility value (*Km*) are given in Table 1, and their related distribution histogram is presented in Figure 5a. For the Pengguan granitic rocks, *Km* mostly varies from 30 μ SI to more than 130 m SI, 65% of the sites have $Km < 1{,}000$ μ SI that is likely originated from paramagnetic carriers, and the rest sites present $Km > 1{,}000$ μ SI and are controlled by ferromagnetic carriers (Rochette et al., 1992).

The representative magnetic mineralogy measurements, including hysteresis loop, isothermal remanent magnetization, and thermomagnetic experiments, are presented in Figure 6 (Detailed nine groups of results are presented in Table S1 and Figure S1 in the supporting information). Most sites display a linear relationship between the applied magnetic field and the induced magnetization (Figure 6a); a quick saturation but a weak intensity of isothermal remanent magnetization (IRM) (Figure 6b) and a sharp drop of *Km* at about 580°C (Figure 6c) indicate that paramagnetic minerals are the principal susceptibility carriers with a weak concentration of the ferromagnetic minerals. A few samples representing a small number of sites are characterized by a nonlinear hysteresis curve (Figure 6d): a quick saturation with a higher intensity of IRM (Figure 6e) and a sharp drop of the *Km* at 580°C (Figure 6f) reveal the presence of magnetite as the main susceptibility carrier. According to the hysteresis curves (Dunlop, 2002), the presence of pseudo single domain (PSD) and multidomain (MD) magnetite has been estimated (Figure 6b). One site showing Cure temperature of approximately 320°C may actually indicate existence of pyrrhotite or gregite (*LM29* in Figure S1).

AGU Tectonics

10.1002/2017TC004754

Table 1
Results of AMS Measurements From the Pengguan Granitic Rocks

	Coordinates			*Km*			K_1				K_3				
Site	Lat (°N)	Long (°E)	*n*	10^{-6}SI	P_j	*T*	Dec (deg)	Inc (deg)	α_{95max}	α_{95min}	Dec (deg)	Inc (deg)	α_{95max}	α_{95min}	Microstructure type
*LM*01	31.278	103.472	5	103	1.046	−0.16	317	70.8	15.8	2.7	142	19.2	4.7	1.5	Strong
*LM*02	31.260	103.482	6	11,000	1.201	0.047	259.3	67.9	8.9	4.3	161.6	3.1	9.9	8.0	Moderate
LM03	31.275	103.474	10	479	1.04	−0.067	336.6	70.8	7.1	4.3	136.6	18.1	8.6	6.5	Moderate
LM04	31.373	103.510	6	208	1.115	−0.136	213.3	72.5	10.7	4.3	100.9	6.8	15.0	4.0	Strong
LM05	31.403	103.527	7	468	1.015	0.076	153.6	71.2	11.3	5.3	257.2	4.5	6.7	2.8	Undefined
LM06	31.182	103.495	7	240	1.066	0.344	19.9	60.7	5.7	5.2	137.5	14.5	13.4	3.3	Undefined
LM07	31.153	103.486	6	138,000	1.378	0.463	67.9	4.7	10.8	3.2	202.5	83.4	5.4	2.7	Magmatic
LM08	31.073	103.487	5	608	1.196	−0.09	274.3	26.8	6.7	3.5	169.4	27	8.5	4.0	Weak
LM09	31.092	103.485	5	679	1.043	0.116	40.7	51.2	8.7	2.0	281.5	21.5	6.6	1.4	Magmatic
LM10	31.111	103.481	5	326	1.032	−0.109	283	22.7	10.8	3.8	16.9	9.3	27.5	5.3	Undefined
LM11	31.073	103.458	7	421	1.008	−0.132	86.2	74	8.5	6.5	288.8	14.9	18.0	6.6	Undefined
LM12	31.077	103.435	9	498	1.078	0.423	259.6	31.1	20.9	6.9	152.9	25.5	8.5	5.1	Weak
LM13	31.061	103.410	8	58,400	1.19	−0.03	91.5	85	7.1	3.3	195.9	1.2	9.2	3.3	Magmatic
LM14	31.063	103.386	8	404	1.116	0.476	49.5	46.7	13.3	3.0	173.9	29.5	12.5	3.8	Weak
LM15	31.066	103.369	7	443	1.042	0.039	52	19.7	9.4	4.5	179.4	59.5	10.2	6.5	Undefined
LM16	31.059	103.347	9	336	1.055	0.127	290.8	37.9	20.0	9.1	183.6	20.9	14.2	5.7	Strong
LM17	31.072	103.324	7	223	1.067	−0.327	344.6	56.6	10.8	1.7	132.2	29.2	12.7	3.4	Undefined
LM18	31.097	103.563	5	68	1.028	0.451	358.7	3.1	16.3	8.8	267.9	14.8	9.2	6.9	Weak
LM19	31.142	103.578	5	466	1.066	−0.012	63.3	69.3	6.7	2.5	177.3	8.8	13.3	3.8	Undefined
LM20	31.118	103.558	5	21,100	1.022	−0.201	338.3	36.8	33.8	0.3	133.5	50.5	16.7	1.1	Magmatic
LM21	31.193	103.653	8	796	1.025	−0.106	294.6	28.7	6.8	5.5	167.9	47.6	57.1	5.8	Undefined
LM22	31.208	103.640	5	1,020	1.038	−0.025	299.3	62.8	17.5	4.5	109.8	26.9	27.3	11.7	Weak
LM23	31.215	103.643	10	1,320	1.06	−0.378	69.2	34.6	15.6	10.1	308.8	36.2	50.5	14.8	Undefined
LM24	31.180	103.658	10	2,330	1.058	0.301	333.3	12.3	32.7	10.7	81.3	54.9	49.4	8.4	Undefined
LM25	31.344	103.880	10	737	1.073	−0.081	246.1	61	13.8	7.3	101.9	24.2	9.5	6.2	Weak
LM26	31.410	103.537	9	448	1.052	0.105	225.7	76	15.2	5.2	327.4	2.9	11.5	4.5	Undefined
LM27	31.395	103.549	5	325	1.047	0.274	21.1	61.1	24.1	2.2	280.3	5.9	19.2	4.6	Undefined
LM28	31.379	103.559	8	974	1.052	0.451	282.3	17.6	12.6	6.7	23.3	31.1	12.3	6.5	Undefined
LM29	31.429	103.574	5	30	1.053	0.145	36.2	75.9	16.6	4.2	143.7	4.3	9.5	3.9	Weak
LM30	31.413	103.588	6	1,250	1.023	0.167	237.2	46.9	36.3	10.0	30.5	39.9	32.1	6.2	Undefined
LM31	31.399	103.603	5	7,720	1.058	−0.198	51.1	68.7	14.1	7.1	176.9	12.9	29.9	7.1	Undefined
LM32	31.308	103.527	5	24,100	1.044	0.08	219.3	60.1	12.0	8.1	124.5	2.8	14.6	7.9	Undefined
LM33	31.291	103.525	8	4,130	1.059	−0.437	332.1	74.3	10.9	6.1	157.2	15.6	64.2	8.1	Undefined
LM34	31.272	103.525	5	89	1.04	−0.378	321.1	78.5	25.1	2.3	86.6	6.7	18.0	6.2	Undefined
LM35	31.271	103.521	7	3,540	1.118	0.153	283.6	79.6	7.8	3.9	166.8	4.8	7.4	1.4	Moderate
LM36	31.264	103.504	6	145	1.072	−0.276	296.7	64.7	15.4	6.7	169.3	16	12.5	6.7	Undefined

Note. Lat: latitude, Long: longitude, *n*: the number of cylinders measured in each site, *Km*: mean magnetic susceptibility, P_J and *T*: anisotropy degree and shape parameter, respectively, K_1 and K_3: magnetic lineation and pole of magnetic foliation, respectively, Inc: inclination, and Dec: declination, α_{95max} and α_{95min}: long and short axes of ellipsoid uncertainty, respectively.

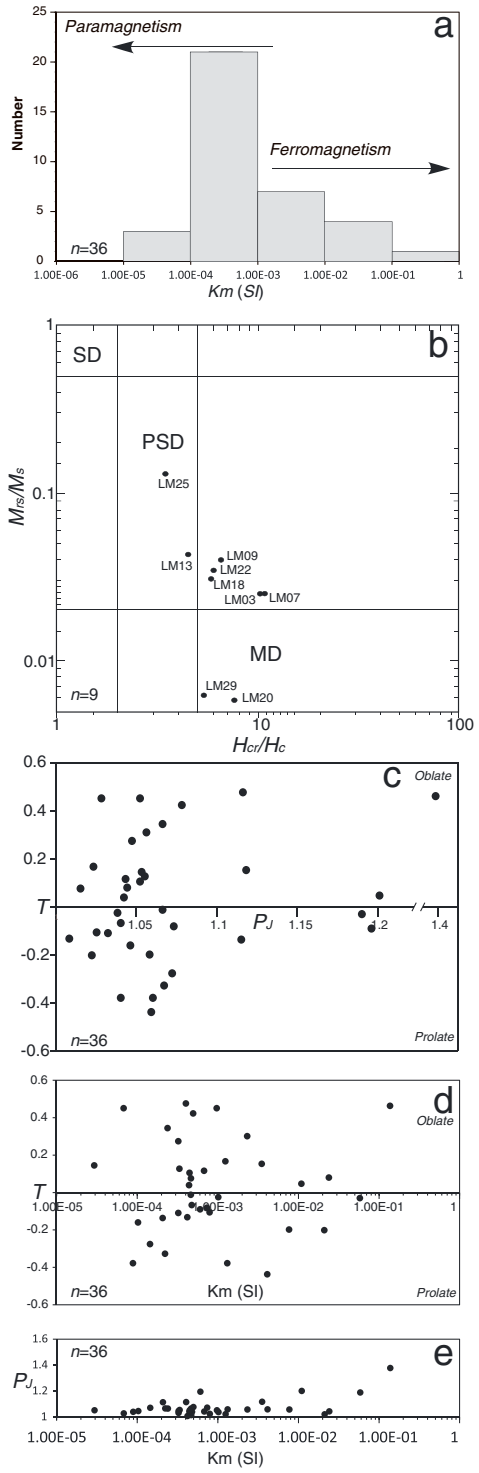


Figure 5. AMS scalar parameters of the Pengguan granodiorite and diorite: (a) histogram of site mean magnetic susceptibility (*Km*). (b) Mrs/Ms versus Hcr/Hc diagram from selected samples of the Pengguan granitic rocks to define the size of magnetite. Mrs: remanence of saturation magnetization after removing the applied field, Ms: saturation magnetization under applied field, Hcr: coercivity of remanence after removing the applied field, Hc: coercivity under applied field, SD: single domain, PSD: pseudu single domain, and MD: multi-domain. (c) Shape parameter *T* versus anisotropy degree P_j value. (d) Bulk magnetic susceptibility *Km* versus shape parameter *T*. (e) Anisotropy degree P_j value versus *Km*.

In summary, the AMS of most samples of the Pengguan granitic rocks is controlled by paramagnetic minerals (phyllosilicates). In these samples, magnetite and Fe-sulfides probably also make minor contribution to their AMS. In a minority of samples the MD/PSD magnetite forms the dominant magnetic carrier. Thus, the magnetic susceptibility carriers of the Pengguan granitic rocks consist of the paramagnetic phyllosilicates, the ferromagnetic magnetite, and the Fe-sulfides (Bouchez & Gleizes, 1995; Bouchez et al., 1997; Kruckenberg et al., 2010; Wei, Martelet, et al., 2014).

4.3. AMS Results

A lack of consistent correlation between P_J, *T*, and *Km* (Figures 5c and 5d) implies that AMS, at least for the paramagnetic susceptibility carrier, varies independently from the magnetic minerals (Borradaile & Henry, 1997). The sites of *LM07* and *LM13* with extremely high P_j could be the result of extremely high susceptibility (Rochette et al., 1992). These sites may be affected by late stage hydrothermal fluid circulation and will be ignored in the following discussion.

The equal-area projection of the magnetic principal axes with their confidence ellipses at 95% level is given in Figure 7. Most magnetic principal axes are well defined with low α_{95max} values (Figure 7 and Table 1). The sites of *LM24* and *LM27* display poorly defined magnetic fabric and will be ruled out in the following discussion. Some fabrics indicate that K_2 and K_3 have a girdle distribution on the same plane that reflects a prolate fabric and corresponds to a negative *T* value (*LM10, 21*, *23*, *31*, and *33*); these sites could be also affected by uniaxial single domain magnetite which displays inverse fabrics (Table 1) (Ferré, 2002).

The orientation contour diagrams of the magnetic fabrics distinguish a prevailing group of foliations dipping steeply to the NW (with an average direction of 53°/76°NW) and lineations plunging steeply to the NW (with an average direction of 45°/75°NW; Figure 8a). The orientation diagrams also reveal a subset of sites with moderately north dipping or steeply east dipping foliations and moderately NE plunging lineations.

Magnetic structures of the complex in map view display that the steeply NW dipping foliations generally associated with the steeply NW plunging lineations are mostly distributed in the NW domain of the complex, while the north dipping foliations and associated moderately NE plunging lineations and other magnetic fabrics having random azimuth are mostly distributed in the SE domain of the complex (Figure 8b). It is worth noting that the AMS fabrics of the NW domain of the complex is consistent with the tectonic fabrics measured in the field.

Specimens cut from samples of five representative sites (*LM01*, *02*, *03*, *15*, and *17*) that had well-clustered magnetic fabrics were selected to evaluate the relationship between the principal AMS directions and macroscopic fabrics observed in the field. The magnetic foliation in all five selected samples corresponds well with the mylonitic foliation measured in the field, and when the lineation could be observed in the field, it corresponds well with the orientation of K_1 (Figures 7 and 8b). In the *XZ* plane thin sections, the magnetic foliation defined by biotite and magnetite is parallel to the field observed foliation (Figures S2a and S2b).

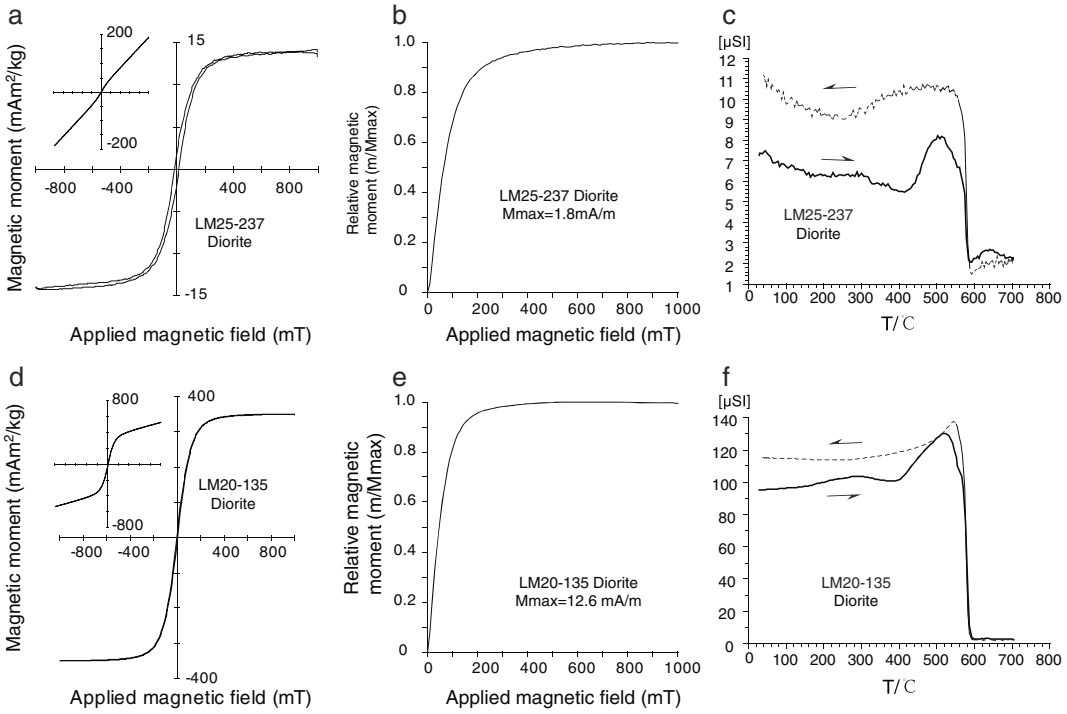


Figure 6. Magnetic mineralogical measurements of representative specimens from the Pengguan granitic rocks. (a, d) Magnetic hysteresis loop diagram (small insects are those before removing paramagnetic component), (b, e) measurements of isothermal remanent magnetization, and (c, f) thermomagnetic experiments of the Pengguan granitic rocks.

4.4. Microstructural Analysis of AMS Samples

Microtextural and microstructural analyses are based on the observation of mineral relationships, subgrains, and intracrystalline microstructures. This is intended to qualitatively assess the deformation of the granitic rocks and to distinguish solid-state fabrics from magmatic fabrics by comparison of the mineral structures with the AMS fabrics (Nédélec & Bouchez, 2015; Paterson et al., 1998, 1989; Sen et al., 2014; Wallis et al., 2014). Twenty-one thin sections coming from 19 AMS sites and 2 hand samples, cut parallel to the magnetic/tectonic lineation and perpendicular to the magnetic/tectonic foliation (*XZ* plane), were observed under the optical microscope. The systematic examination on these thin sections allowed us to discriminate four types of microstructures including (i) magmatic, (ii) weak solid-state, (iii) moderate solid-state, and (iv) strong solid-state microstructures. The samples experienced the strong solid-state deformation will serve to discuss the kinematics with respect to their spatial distribution in the complex.

1. *Magmatic microstructure*. The magmatic microstructure does not exhibit visible solid-state deformation. Despite the plagioclase partially altered to sericite, the rock primary structures are defined by well-preserved euhedral amphibole, weak undulose extinction in quartz, and euhedral pseudomorphose of feldspar depicted by sericite aggregates (Figure 9a). The amphiboles with a rhombic shape are randomly distributed in the groundmass of quartz and feldspar with magmatic microstructures. Biotite grains, with sharp boundaries, are neither kinked nor bent.
2. *Weak solid-state microstructure*. The quartz grains have undulose extinction and subgrain walls are developed (Figure 9b). Quartz-quartz boundaries are lobate or slightly serrated, and small newly formed grains appear with the same grain shape preferred orientation, arguing for the onset of dynamic recrystallization. Biotite grains are slightly elongated due to glide along their basal plane. Such a microstructure indicates that some deformation took place during the transition from magmatic to solid state.
3. *Moderate solid-state microstructure*. Moderate solid-state microstructure is attested by the ubiquitous serrated grain boundaries and uniform grain size that replace the primary quartz grains with slight differences in extinction of the quartz. Subgrain rotation becomes the main dynamic recrystallization mechanism in quartz (Figure 9c). The biotite grains record extensive kinking and the feldspars display obvious fractures (Figure 9d).

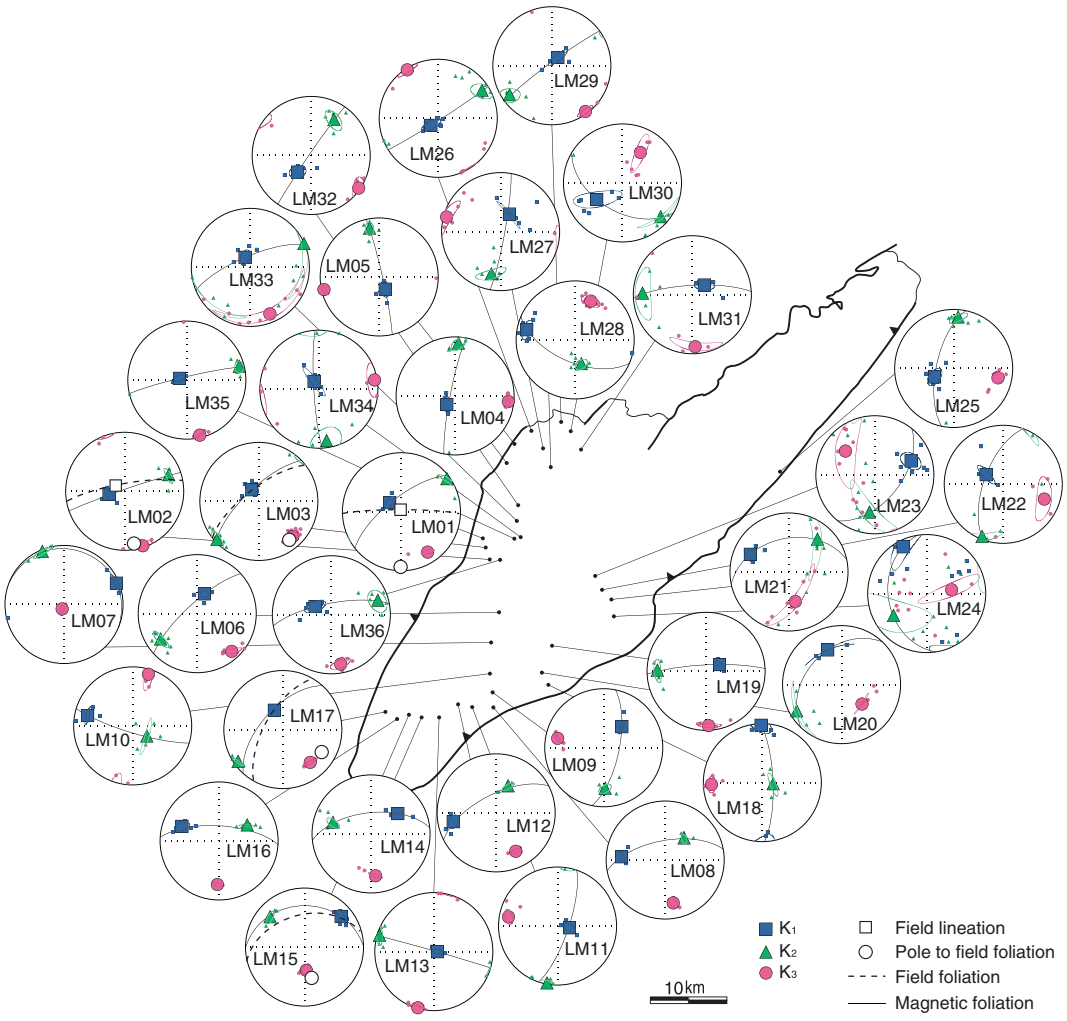


Figure 7. AMS fabrics for each site of Pengguan granitic rocks and compare to the field measured fabrics. K_1: magnetic lineation and K_3: pole of magnetic foliation. All projections are equal area lower hemisphere.

4. *Strong solid-state microstructure*. In the intensive solid-state deformation microstructures, the aggregates and recrystallized grains display obvious mylonitic characteristics, such as quartz ribbon, sigmoidal mica aggregates (Figure 9e), fine-grained quartz, and feldspar form tails around residual feldspar phenocrysts (Figure 9f).

Although merely 21 sites were conducted for microstructural observations for the whole Pengguan complex, the above defined types of deformation state display a well-defined distribution (Figure 8c). The moderate and strong solid-state deformed microstructures are exclusively distributed in the NW domain of the complex, while the weak solid-state and magnetic fabrics are distributed in the SE domain.

4.5. Interpretation of AMS and Microstructures of the Pengguan Granitic Rocks

The magnetic susceptibility of the Pengguan granitic rocks mostly arises from paramagnetic biotite and partly ferromagnetic magnetite (PSD or MD) based on *Km*, thermomagnetic, hysteresis loop, and isothermal remanent magnetization measurements. Numerous previous studies have demonstrated that paramagnetic minerals and ferromagnetic minerals carry comparable magnetic fabrics with the mineral petrofabrics in terms of orientation (Borradaile & Jackson, 2004; Bouchez & Gleizes, 1995; Bouchez et al., 1997; Parsons, Ferré, et al., 2016; Rochette et al., 1992]. Stereonet projection and microscopic characteristics indicate that the well-clustered magnetic fabrics of the mylonitic samples within the Pengguan complex are consistent

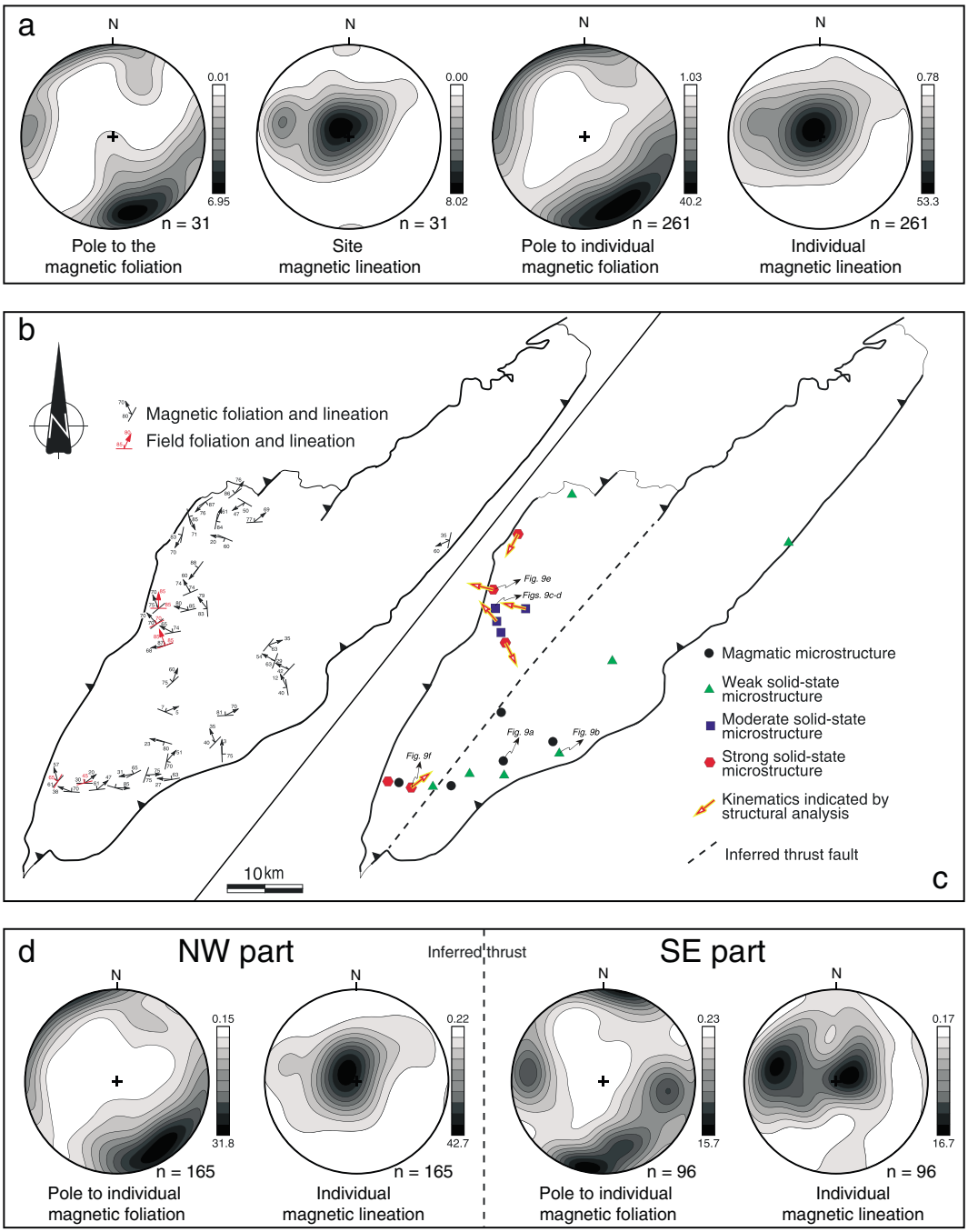


Figure 8. Data analysis after removing the extremely high *Km* sites of *LM07*, *13* and poorly defined sites of *LM23*, *24*, and *27*. (a) Orientation contour diagrams of site mean and individual magnetic fabrics. (b) Site mean magnetic and field fabrics of the Pengguan complex. (c) Deformation intensity zonation based on microstructural study. (d) Orientation contour diagrams of individual magmatic fabrics partitioning based on deformation zonation. All projections are equal area lower hemisphere.

with the field observed fabrics (Figures 7, 8b, S2a, and S2b). Thus, the subfabrics of the biotite and magnetite of the Pengguan granitic rocks contribute to the normal magnetic fabrics.

The well-grouped magnetic fabrics characterized by steeply NW dipping foliations and steeply NW plunging lineations, from these rocks with moderate solid-state deformation, are consistent with those from ductilely deformed fabrics as well as the regional field fabrics, which are mostly distributed in the NW domain of the

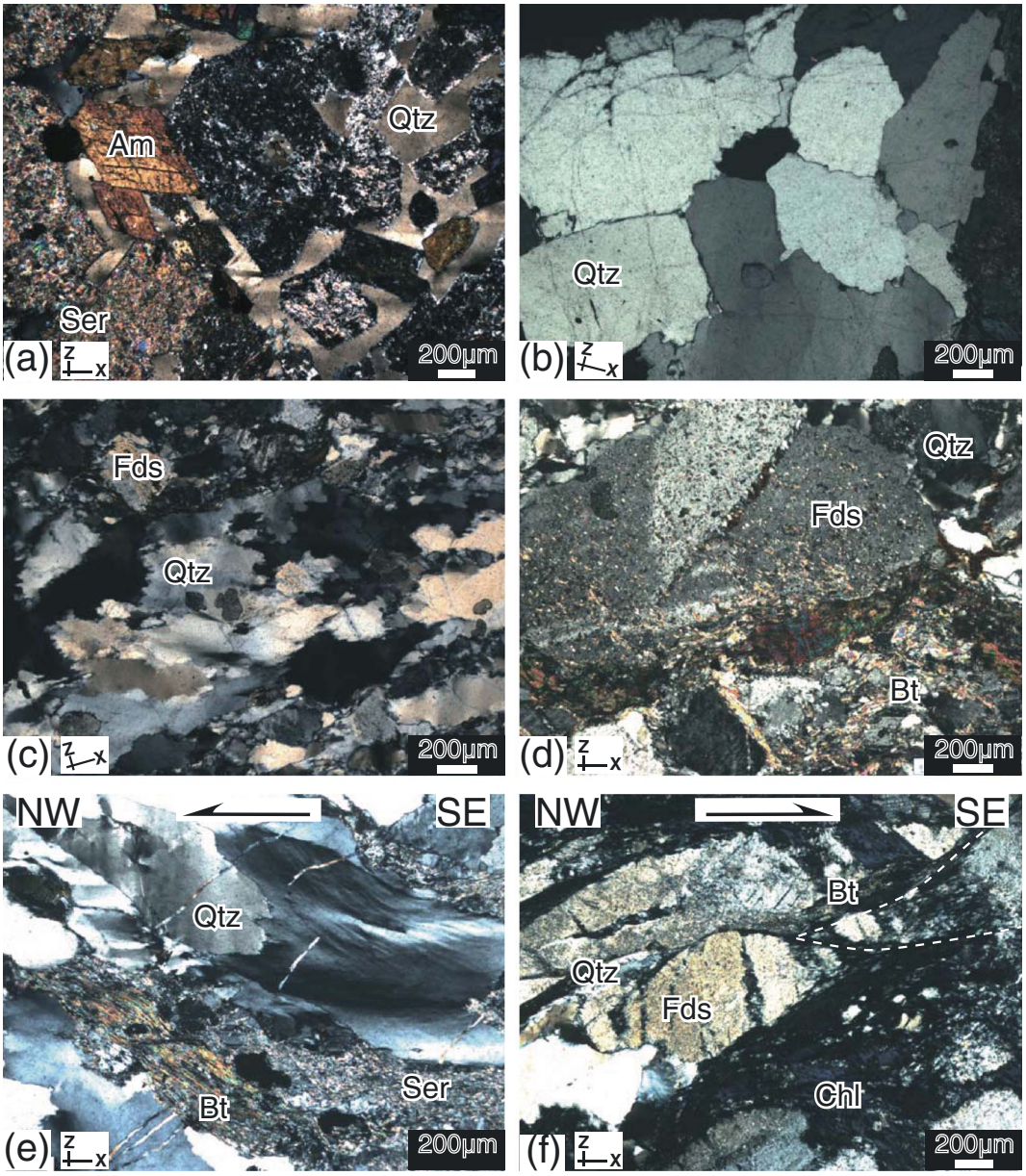


Figure 9. Microstructures observed in the granitic rocks of the Pengguan complex. (a) Magmatic microstructures with euhedral amphiboles and altered plagioclase grains (31°16.661′N, 103°28.322′E). (b) Weak solid-state deformation, lobate quartz boundaries, and a few buldging neograins indicate partial recrystallization (31°05.812′N, 103°33.763′E). Moderate solid-state deformation: (c) quartz-quartz serrated boundaries and recrystallization with similar grain shape preferred orientation, subgrain rotation is the dominant recrystallization mechanism (31°16.661′N, 103°28.321′E). (d) Feldspars flexured like sand clock with biotite and chlorite wrapped around (31°16.661′N, 103°28.321′E). Intensive solid-state deformation: (e) Recrystallized quartz grains organized into ribbons and mica aggregates form sigmoidal structures that indicate top-to-the-NW shearing (31°22.391′N, 103°20.848′E). (f) Fine-grained quartz and feldspar forming tails around residual feldspar phenocrysts that indicate top-to-the-SE shearing (31°03.536′N, 103°30.588′E). *X* and *Z* axes are marked on the figures. Qtz: quartz, Cal: calcite, Bt: biotite, Ms: muscovite, Ser: sericite, Am: amphibole, Chl: chlorite, and Fds: feldspar.

Pengguan complex, while the SE domain of the complex, characterized by magmatic and weak solid-state microstructures, displays randomly oriented magnetic fabrics (Figure 8d). Thus, it is reasonable to suggest that most of the magnetic fabrics of the NW domain of the complex arise from ductile deformation.

In addition to the kinematics described in section 3.2, the asymmetric quartz ribbon, the sigmoidal structures of micas and feldspars on thin sections (perpendicular to the field foliation and parallel to the magnetic

lineation) indicate both top-to-the-NW and top-to-the-SE shearing in the NW domain of the Pengguan complex (Figures 8b, 9e, and 9f). The mineral assemblage that defines the foliation includes quartz + feldspar + biotite + chlorite; it suggests that the top-to-the-SE shearing occurred under greenschist facies metamorphism conditions, which is similar in metamorphic grade to the metamorphism in the NW boundary of the complex (Figures 4 and 9f). Both top-to-the-NW shearing and top-to-the-SE shearing are accommodated with quartz subgrain rotation dynamic recrystallisation, which also support the greenschist facies metamorphism (Figures 4 and 9f).

5. Gravity Modeling

Gravity modeling has long been used to depict the bulk architecture of deep structures; it is especially well suited to decipher the geometry of plutonic massifs (e.g., Bolle et al., 2002; Guineberteau et al., 1987; Lin et al., 2013; Talbot et al., 2005; Turrillot et al., 2011; Wei, Martelet, et al., 2014). In order to complement our field structural and AMS observations, we applied this approach to constrain the deep structure of the Pengguan complex and adjacent areas.

5.1. Gravity Map

In the study area, a detailed Bouguer anomaly map (1,200000) was acquired from the Geological Survey of China, complemented regionally by a lower-resolution (2′ × 2′) Bouguer grid acquired from the International Gravimetric Bureau database (Bonvalot et al., 2012). In order to highlight the short wavelengths gravity signatures of the upper crust, the long wavelengths gravity anomaly were subtracted from the complete Bouguer anomaly at the regional scale. After several trials, the regional component was extracted using a low-pass Butterworth filter with a 70 km cutoff, which (i) fitted well the gravity trends at the regional scale and (ii) properly outlined residual anomalies over known outcropping geological structures. In Figure 10, main geological boundaries are superimposed on the residual gravity anomaly map (BGMRSP, 1991).

The general architecture of the residual gravity map is structured along three main NE-SW trending units: in the center, the LMTB predominantly outlined by high gravity anomalies, separates the Sichuan foreland basin to the SE, marked by well-defined low gravity anomalies, and the SGT to the NW, marked by intermediate gravity signatures. In the residual anomaly, several Mesozoic granites intruded in the SGT display well-defined negative anomalies due to their low density relative to the country rocks (Figure 10). A significant positive anomaly appears at the position where the Pengguan complex is located (Figure 10). To the northwest of the Pengguan complex and nearly parallel to the LMTB, there is a well-defined positive gravity anomaly belt, which does not associate with any outcrop of high-density material (Figure 10).

5.2. Two-Dimensional Gravity Modeling

To feature the deep geometry of the Pengguan complex and the LMTB, 2-D gravity modeling was performed. Two NW-SE trending profiles perpendicular to the LMTB were modeled using Geosoft-GM-SYS software (Figure 10). Density of rocks considered in the modeling is derived partly from laboratory measurements. We concentrated our density determinations on rocks outcropping in the Pengguan complex and surrounding areas (Figure 11) and complemented our data set with densities from a previous study for the more peripheral or nonoutcropping geological units (Zhang et al., 2009). For nonoutcropping deep units, the density of the undifferentiated upper crust was chosen at 2.72 g/cm^3 following Turrillot et al. (2011), and we considered the existence of a deep low-density material (density 2.65 g/cm^3) imbricated with the Pengguan rocks that we discuss in a next stage. We also took into account very dense basic/ultrabasic material (density 3.0 g/cm^3) intercalated in the Pengguan complex. This is consistent with the NE-SW trending diabase/gabbro intrusions (circa 195–186 Ma) reported in the Pengguan complex (Figures 2a and 3c) (Chen et al., 2015). Also, we assumed that the NE-SW trending hidden high-density belt northwest of Pengguan complex share the same density as the Pengguan complex. In our profiles, the overall tectonic style and structural dips were made consistent with surface geological observations and information available in nearby seismic profiles. In particular, the three main listric thrust faults were constrained by the seismic reflection data, two of them bound the Pengguan complex (Feng et al., 2015; Guo et al., 2013; Jia et al., 2006; Li et al., 2010).

5.3. Interpretation of the Gravity Model

In Figure 11, the two modeled gravity profiles display similar geological architectures that portray the western Sichuan foreland basin and the SGT, taking into account the overall strata thicknesses constrained by

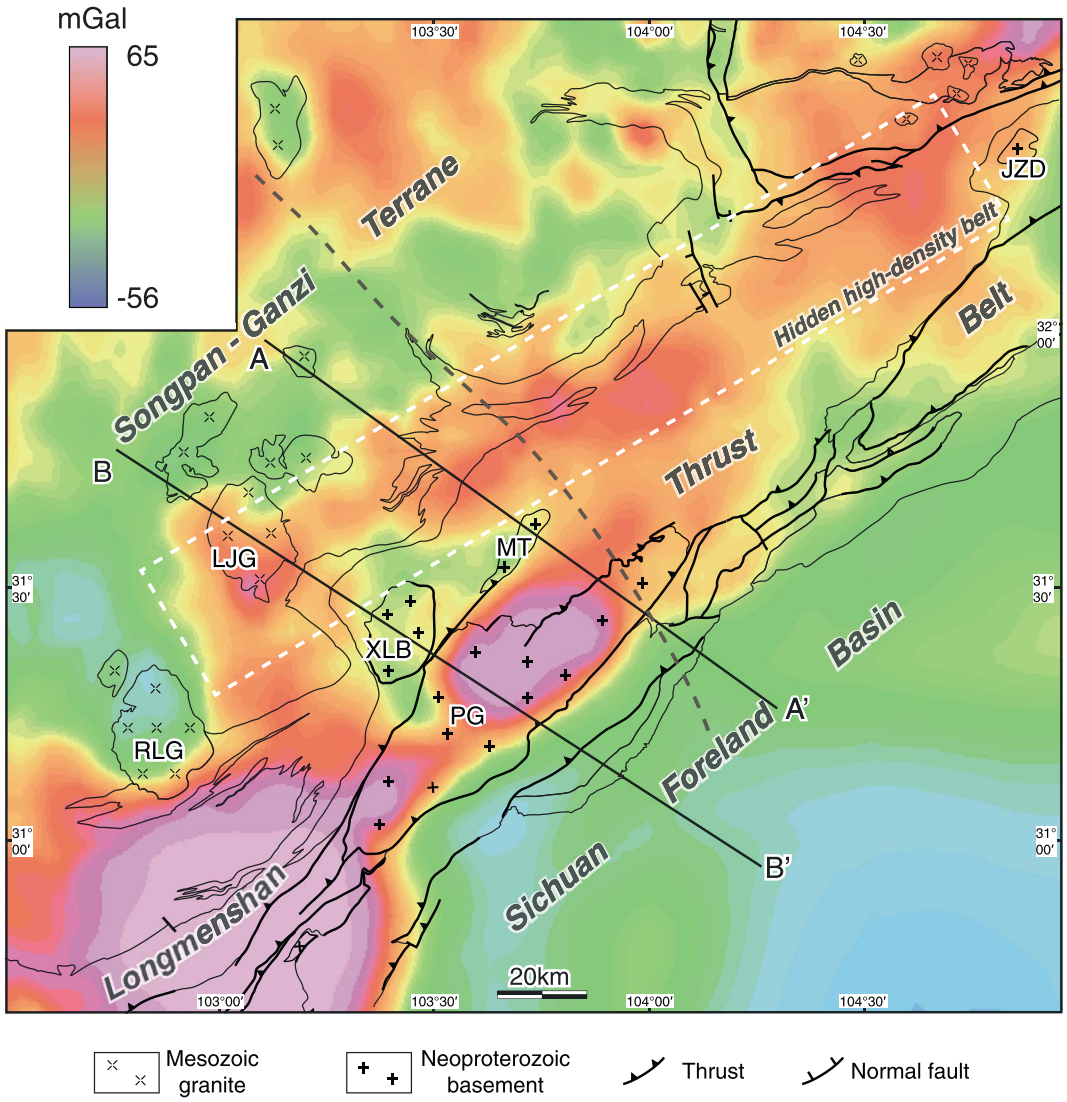


Figure 10. Residual Bouguer gravity anomaly of the Pengguan complex and adjacent areas after subtraction of a 70 km wavelength regional trend from the complete Bouguer anomaly. Gray dashed line represents the location of the seismic profile processed by Guo et al. (2013). PG: Pengguan complex, XLB: Xuelongbao complex, MT: Moutuo complex, JZD: Jiaoziding complex, RLG: Rilonguan granite, and LJG: Laojungou granite.

regional geological mapping (BGMRSP, 1991). According to our models, the SGT, intruded by several Mesozoic plutons, is underlain by dissected basement, while the strata in Sichuan basin are rather flat, as shown in the seismic profile (Figure 11c) (Feng et al., 2015; Guo et al., 2013). In our models, on both sides of the Pengguan complex, the significant thickening of certain sedimentary units is interpreted as the result of folding and thrusting due to the bulk shortening in the LMTB since the Late Triassic. The simplified density applied in the modeling could also partly contribute to the variations in strata thickness. The gravity modeling suggests that the Xuelongbao complex is a 2–3 km thick rootless batholith and the Moutuo complex is even thinner (Figure 11). On the contrary, the Pengguan complex is thick (approximately 20 km), which is partly due to tectonic stacking, according to the gravity model (Figure 11).

The gravity model suggests that the Pengguan complex is strongly tectonized and the NW domain of the complex is underlain by low-density materials, likely implying that a thrust fault separates the NW domain from the SE domain of the complex. This structure is consistent with the zonation of the AMS fabrics and microstructures (Figures 8b–8d and 11). In accordance with the structural observations, the profiles suggest that the NW domain of the Pengguan complex is an allochthonous basement slice, thrusted southeastward

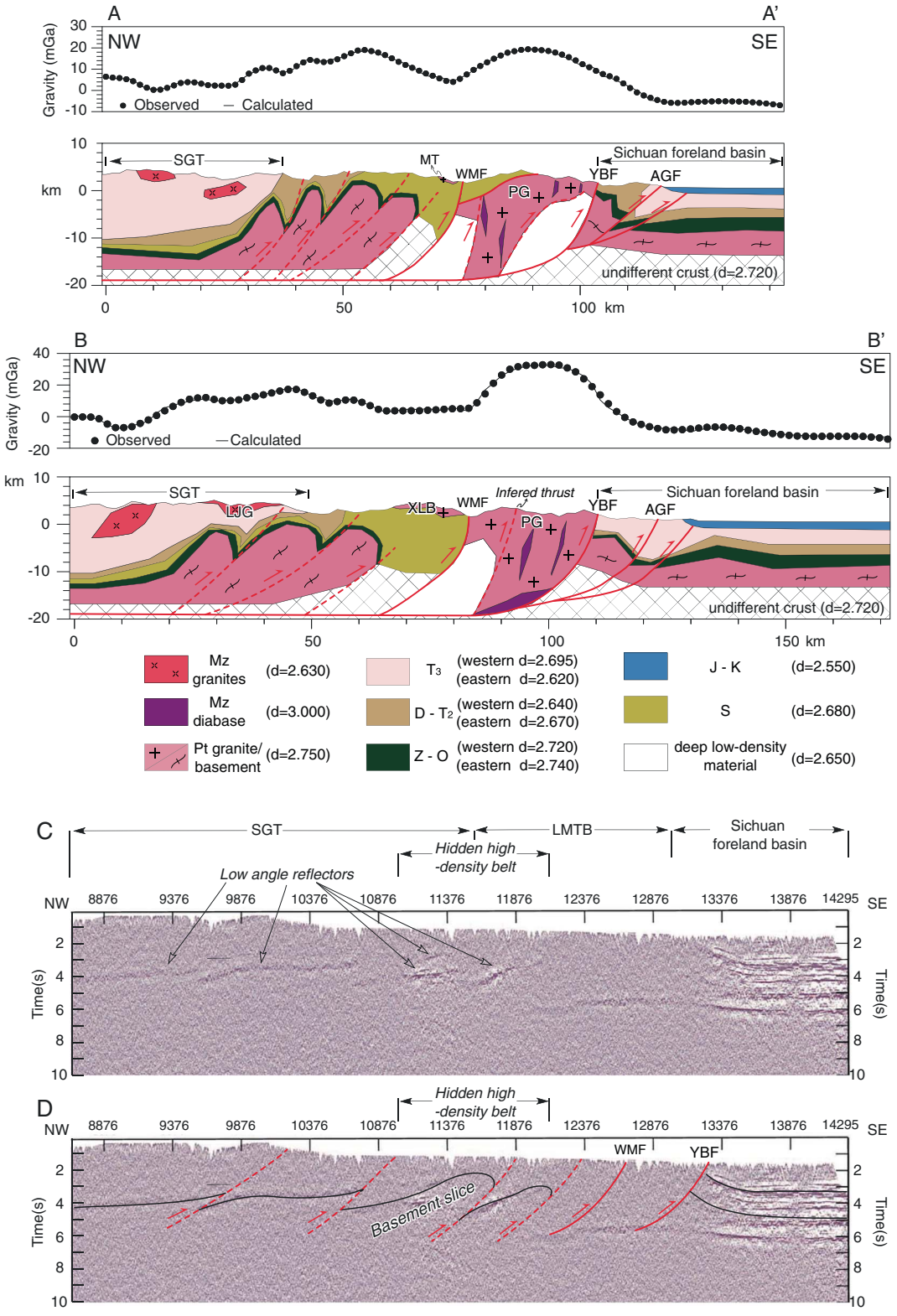


Figure 11. (a and b) Forward gravity models across the LMTB range. The effect of the model, represented by the black continuous line, matches the observed residual Bouguer gravity values represented by the black dots. (c) Seismic profile processed by Guo et al. (2013). (d) Schematic reinterpretation of the seismic profile. Location of these profiles are marked in Figure 10. Thick red lines refer to the thrust faults constrained by seismic reflection data. The dashed red lines represent interpreted thrust faults. Symbols and acronyms are the same as in Figure 1.

onto the autochthonous SE domain. Further to the NW, the hidden high-density belt is considered as an equivalent of the Pengguan complex, but still not outcropping, strongly tectonized and folding the overlying Paleozoic sediments. The gravity model indicates that this high-density belt is associated with an undulated residual Bouguer anomaly, and we match this gravity pattern featuring a series of imbricated basement slices (Figure 11). Either thrusting or normal movement could form such stacked structure. We favor the thrusting as a result of compressional tectonics because field observations show exclusively compressional structures in the study area (Burchfiel et al., 1995; Worley & Wilson, 1996; Xu et al., 1992).

Two possible reasons could account for the low-density material right upon the YBF featured in profile A-A′: (i) low-density Late Triassic sediments tectonically imbricated with granitic rocks during thrusting (Lu et al., 2014) and (ii) the indirect effect due to relatively less mafic intrusions inside the northeastern Pengguan complex compared to its southwestern part (Figure 11).

6. Discussion

6.1. Summary of Our New Results

Our microstructural analysis of the Pengguan complex classified four types of microstructures: magmatic microstructure, weak solid-state microstructure, moderate solid-state microstructure, and strong solid-state microstructure. The latter two types of microstructures, indicating of ductile deformation, are mostly developed in the NW domain of the Pengguan complex and are absent in its SE domain. The AMS fabrics of the ductilely deformed NW domain display steeply NW dipping foliations associated with steeply NW plunging lineations, which are consistent with the field-observed fabrics. The SE domain displays north dipping foliations associated with lineations moderately plunging to the NE or randomly oriented magnetic fabrics (Figures 8b–8d). Thus, the ductile deformation in the NW domain was strong enough to erase the primary magmatic fabrics. Based on kinematical and petrological studies, top-to-the-NW and top-to-the-SE shearing during greenschist facies metamorphism occurred along the NW and SE boundary of the NW domain of the Pengguan complex (Figure 8b). These observations let us suppose that the NW and SE domains of the complex are separated by a thrust fault. The NW domain of the complex acted as an allochthonous basement slice that imbricated southeastward and overlaid the autochthonous SE domain (Figures 2b and 8c).

Two orogen-perpendicular gravity profiles reveal that (i) the imbricated slices of the Pengguan complex are consistent with the AMS and microstructural study, (ii) the base of the Sichuan foreland basin is rather flat while the base of the SGT is dissected, and (iii) northwest of the Pengguan complex, high-density material (basement) concealed by the Paleozoic rocks display the same thrusted/imbricated pattern as the Pengguan complex (Figure 11). In summary, the data presented in this work document a SE verging basement-slice-imbricated structure of the Pengguan complex and adjacent areas.

6.2. Lateral Extent of the Basement-Slice-Imbricated Structure

A high-resolution seismic profile across the LMTB has been processed by Guo et al. (2013) (Figures 10 and 11c). The base of the SGT and of the Sichuan foreland basin interpreted in the seismic profile is consistent with our gravity profiles. In the seismic profile, an echelon arrangement of reflectors moderately dipping to the NW corresponds to the place where the hidden high gravity anomaly belt is located (Figures 10 and 11c). These reflectors were previously interpreted as pop-up and back thrust structures (Guo et al., 2013). However, the reflectors in the seismic profile can be re-interpreted as southeastward imbrication of basement slices, in agreement with our gravity profiles (Figure 11d). Furthermore, the relatively flat reflectors of the SGT are dissected and benched as well.

At the local scale of the Pengguan complex, the top-to-the-NW shearing and the top-to-the-SE shearing control the southeastward basemen-slice imbrication of the NW domain of Pengguan complex. At the regional scale, the top-to-the-NW/N shearing that affects the Pengguan complex extends from the north of Danba dome, across the north of Kangding complex and the Baoxing complex and may extend to the Jiaoziding complex, totalizing more than 300 km in length (Figure 1a) (Burchfiel et al., 1995; Li, 2009; Tian et al., 2016 ; Xu et al., 2008). Thus, it is likely that a belt of imbricated basement slices represented by the orogen-parallel Neoproterozoic complexes is regionally developed along the LMTB. Combining the gravity anomaly residual and the seismic profile, another belt of imbricated basement slices

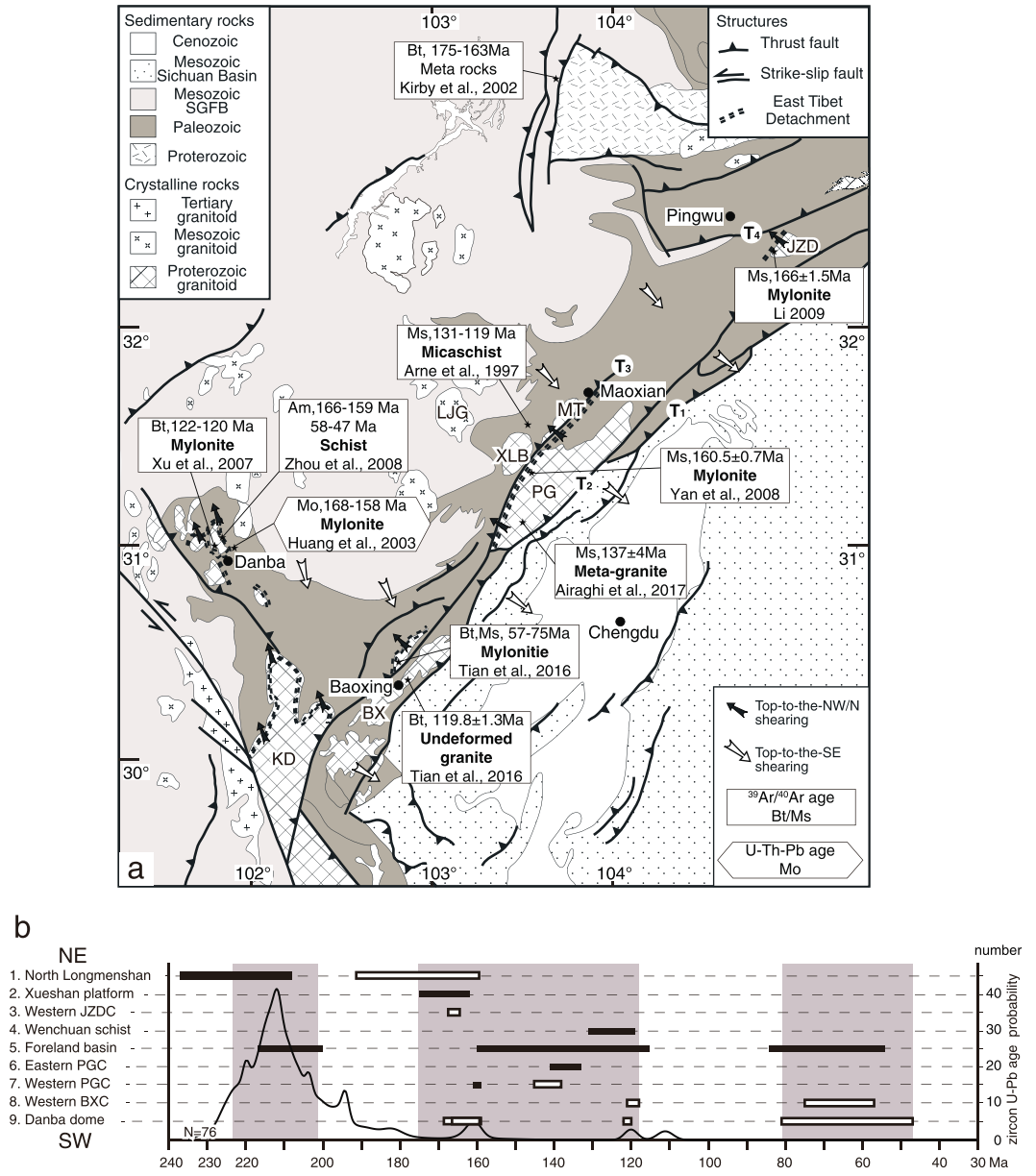


Figure 12. (a) Kinematic map of the Pengguan complex and adjacent area with the compilation of previously published geochronological results. (b) $^{39}Ar/^{40}Ar$ ages from along the LMTB and zircon age probability diagram of the Mesozoic igneous rocks in the SGT. Black rectangle represents samples from the top-to-the SE/S shearing domain; white rectangle represents samples from the top-to-the N/NW shearing domain. Curve represents the zircon age probability diagram of the Mesozoic igneous rocks in the SGT. (1) Yan et al., 2011, (2) Kirby et al., 2002, (3) Li, 2009, (4) Arne et al., 1997, (5) Li et al., 2013, (6) Airaghi et al., 2017, (7) Yan et al., 2008, and Dirks et al., 1994, (8) Tian et al., 2016, and (9) Huang, Buick, et al., 2003, Zhou et al., 2008, and Xu et al., 2008. Symbols and acronyms are the same as in Figure 1.

represented by the hidden high-density material that may be regionally developed on the west of the LMTB as well. These two parallel belts of imbricated basement slices therefore constitute the LMTB and adjacent areas (Figure 10).

6.3. Geochronological Constraints

Published $^{39}Ar/^{40}Ar$ ages measured along the LMTB, on biotite, muscovite, amphibole, and U-Th-Pb dating on monazite from mylonites and micaschists are presented in Figure 12a, and these ages can be roughly divided into three periods (Figure 12b). The first period from 237 to 200 Ma and the third period from 81 to 47 Ma

correspond, respectively, to the Early Mesozoic and Late Cretaceous-Cenozoic shortening in the LMTB. The zircon ages of the granites in the SGT reveal one predominant peak at circa 211 Ma that postdates the Early Mesozoic shortening (Figure 12b) (BGMRSP, 1991; Hu et al., 2005; Roger et al., 2004; Sigoyer et al., 2014; Xiao et al., 2007; Zhang et al., 2006).

The second group of $^{39}Ar/^{40}Ar$ ages span over a large time period between 175 and 118 Ma (Figure 12). For the belt displaying top-to-the-NW/N shearing distributed at the NW/north boundary of the Neoproterozoic complexes, the recrystallized biotite and muscovite from the NW boundary of the Jiaoziding complex involved in NW shearing yield an $^{39}Ar/^{40}Ar$ age of circa 166 Ma (Li, 2009). The ages between 168 and 158 Ma dated by $^{39}Ar/^{40}Ar$ method on amphibole and U-Th-Pb one on monazite from mylonite and micaschists in the north of the Danba dome were interpreted as the timing of top-to-the-N/NW shearing (Huang, Maas, et al., 2003; Zhou et al., 2008). Younger biotite $^{39}Ar/^{40}Ar$ dating ages, at circa 120 Ma, have also been reported at the northwest boundary of the Baoxing complex and the north boundary of the Danba dome, which were interpreted as cooling ages (Tian et al., 2016; Xu et al., 2008). For the top-to-the-SE shearing, the ages of 166–140 Ma yielded by $^{39}Ar/^{40}Ar$ dating on muscovite from the Pengguan mylonitic rocks were interpreted as the age of muscovite recrystallisation during the top-to-the-SE shearing (Airaghi et al., 2017; Yan et al., 2008). In the west of the Pengguan complex, $^{39}Ar/^{40}Ar$ dating on the deformed muscovite from micaschists involved in the top-to-the-SE shearing yields ages between 131 and 119 Ma, which are also interpreted as the timing of the top-to-the-SE shearing (Arne et al., 1997). The flexural subsidence in the Sichuan foreland basin occurred during J_3-K_1 is also interpreted as the consequence of the SE thrusting and loading of the LMTB (Dirks et al., 1994; Li et al., 2013). Thus, the top-to-the S/SE shearing and the top-to-the N/NW shearing that control the imbrication of the basement slices occurred during J_3-K_1.

Detailed geochronology studies on the metamorphic and magmatic rocks of the SGT indicates a slow regional cooling history during 203–30 Ma (Huang, Buick, et al., 2003; Huang, Maas, et al., 2003; Roger et al., 2011). Meanwhile, the Mesozoic Laojungou granite (224 ± 5 Ma) in the SGT experienced a rapid exhumation between 172–140 Ma (Yuan et al., 1991; Zhao, 2007). The Laojungou granite was probably popped up by the imbrication of the underlying basement slices, resulting in localized fast exhumation (Model B–B′ in Figure 11). This was contemporary to the localized fast exhumation (168–158 Ma) recorded in the Danba area (Huang, Maas, et al., 2003).

In Figure 12b, the zircon age distribution of the granites in the SGT also displays two weak peaks at circa 162 and circa 120 Ma, which could be the magmatic response to the imbrication of the basement slices. In summary, we argue that this basement-slice-imbricated structure formed during the Late Jurassic-Early Cretaceous times.

6.4. Evolution Model of the LMTB and Its Tectonic Implications

Several models have been invoked to interpret the emplacement of the orogen-parallel Neoproterozoic complexes and associated top-to-the-NW/N shearing (Burchfiel et al., 1995; Li, 2009; Tian et al., 2016; Xu et al., 2008; Zhou et al., 2008). The crustal wedge extrusion or lower crust flow bounded by a thrust on the foreland side and a normal fault on the hinterland side has been suggested (Burchfiel et al., 2008; Xu et al., 2008). In the model of crustal wedge extrusion, an extensional basin would be expected in the hanging wall side of the normal fault, whereas, no basin has been reported in the hinterland of the LMTB. The lower crust flow model, alike the Himalayan with the Main Boundary Thrust and South Tibetan Detachment, considers that the partially melted lower crust is driven by the topographic loading and surface denudation (Beaumont et al., 2001). However, the partially melted material, such as the leucogranitic magmatism in south Tibet, is absent in the LMTB. Another crust duplex model under contractional tectonics has been proposed to explain the southwestern LMTB (Tian et al., 2016) but failed to explain the top-to-the-NW shearing and the imbrication of the Neoproterozoic basement. All three models mentioned above did not incorporate the belt of imbricated basement slices in the SGT.

The imbricated Neoproterozoic complex and the hidden imbricated structure lead us to propose a basement slice imbrication model. One belt of basement slices is exposed on the surface as the orogen-parallel Neoproterozoic complexes, while the other belt of basement slices is concealed on the west of the LMTB. Figure 13 presents a general evolution scenario of the LMTB and adjacent areas. A pre-Middle Triassic rift was developed along the western boundary of the SCB proposed by Long (1991) and Chen and Wilson (1996),

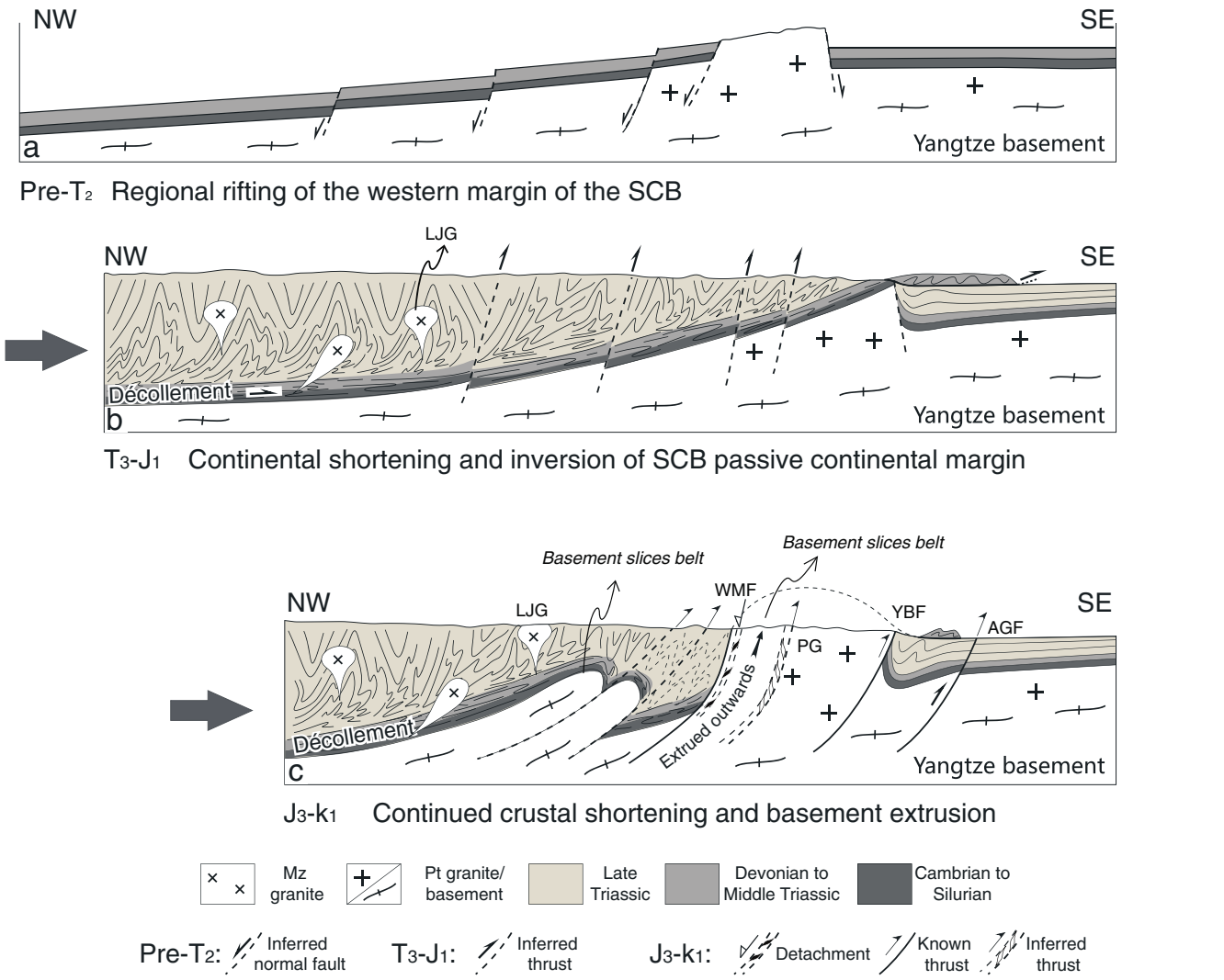


Figure 13. A possible evolution scenario of the LMTB. (a) A pre-middle Tricassic rift along the South China Block (SCB). (b) During the Late Triassic-Early Jurassic continental shortening and inversion of SCB passive continental margin. (c) During the Late Jurassic-Early Cretaceous, continued crustal shortening and basement slice extrusion. The symbols and acronyms are the same as in Figure 1.

and numerous NW dipping normal faulting were developed in accommodation with this extension (Figure 13a). During T_3-J_1, the Mesozoic shortening led to large-scale southeastward thrusting and folding of the Paleozoic-Triassic formation of the SGT, along a regional décollement located in the low-strength Silurian shale and pelite, and the latter was transported southeastward to the Sichuan foreland basin as nappes (Burchfiel et al., 1995; Calassou, 1994; Roger et al., 2004; Xu et al., 1992). At the same time, the early NW dipping normal faulting developed along the passive margin of the South China Block was inverted and cut the basement of the Longmenshan area into a step-like shape (Figure 13b) (Burchfiel et al., 1995; Chen & Wilson, 1996; Long, 1991). These crustal thickening and shearing events were responsible for the widespread intrusion of granites in the SGT and the initiation of the Sichuan foreland basin (Calassou, 1994; Harrowfield & Wilson, 2005; Hu et al., 2005; Roger et al., 2004; Sigoyer et al., 2014).

During J_3-K_1, the basement was cut into slices by several faults and transported southeastward probably due to the collision between the Lhasa and Qiangtang Blocks (Figure 13b) (Yin & Harrison, 2000). One belt of imbricated basement slices represented by the Jiaoziding, Pengguan, Baoxing, Kangding complexes, and the Danba dome is located in the proximal continental margin of the Yangtze Block, part of the SCB. These slices accumulated the highest strain and were "squeezed" outward, which formed the contemporaneous top-to-the-NW shearing and top-to-the-SE shearing along their NW and SE boundaries, respectively

(Figure 13c). The other belt of basement slices underlies and sustains the SGT so that no extensional basin developed at the hanging wall side of the NW normal fault (Figure 13c).

Coeval top-to-the hinterland shearing and top-to-the foreland thrusting are generally developed in orogens with thickened crust though their thickening mechanisms are fundamentally in variance, such as in the southeastern Canadian Cordillera (Price, 1986), the Alpine orogen (e.g., Schmid et al., 2004; Selverstone, 2005; Tavarnelli, 1999), the Late Devonian Appalachians (e.g., Castonguay et al., 2007; Pinet et al., 1996), the Scandinavian Caledonides (e.g., Grimmer et al., 2015; Hartz & Andresen, 1997), and the central East Greenland Caledonides (e.g., Johnston et al., 2010; White & Hodges, 2002). It is therefore reasonable to suggest that the Longmenshan crust had reached a significant thickness by the Late Jurassic-Early Cretaceous, probably due to the imbrication of basement slices. This inference is consistent with the contemporaneous development of Barrovian metamorphism west of the WMF and migmatization north of the Danba dome (Arne et al., 1997; Dirks et al., 1994; Huang, Maas, et al., 2003). Inverse multiequilibrium thermodynamic approach and in situ $^{39}Ar/^{40}Ar$ dating indicate that the Pengguan complex was exhumed from approximately 20 km depth and overprinted by greenschist facies metamorphism during 135–140 Ma (Airaghi et al., 2017). On the base of the results illustrated above, the imbrication of basement slices in the Longmenshan belt at least resulted in the crustal thickening more than 20 km in thickness along the NE Tibet in Late Mesozoic times, which contradicts to the previously proposed Cenozoic thickening models.

7. Conclusions

Structural analysis, AMS measurements, petrofabric study, and gravity modeling reported in this study reveal that the bulk architecture of the LMTB and adjacent areas consists of two parallel belts of SE imbricated basement slices. One belt of the basement slices close to the Yangtze Block is bounded by the top-to-the-NW/N and top-to-the-SE shearing that formed the Pengguan complex and other orogen-parallel Neoproterozoic complexes. The other belt of imbricated basement slices underlies the SGT and sustains its high topography.

The previously published geochronological data, the localized fast exhumation rate, and lithological characteristics of sediments in the Sichuan foreland basin indicate that the imbrication of the basement slices occurred during Late Jurassic-Early Cretaceous. We therefore suggest that the LMTB experienced a significant phase of basement slices imbrication, crustal thickening, and associated exhumation in the Late Mesozoic times; consequently, this may imply that the importance of deformation and exhumation in the Cenozoic of this area is often overestimated.

Acknowledgments
We are indebted to Andrew Parsons and Jean-Luc Bouchez for their constructive advices and criticism. This work is financially supported by the MOST project of China (2016YFC0600401 and 2016YFC0600102) and NSFC project (41472193 and 41225009). Zhenhua Xue is grateful to Hongsheng Liu for gravity modeling assistance. The data for this paper are available as supporting information Table S1 and Figures S1 and S2, and any further information can be obtained upon request.

References

Airaghi, L., Sigoyer, J. D., Lanari, P., Guillot, S., Vidal, O., Monié, P., … Tan, X. (2017). Total exhumation across the Beichuan Fault in the Longmen Shan (eastern Tibetan Plateau, China): Constraints from petrology and thermobarometry. *Journal of Asian Earth Sciences*, *140*, 108–121. https://doi.org/10.1016/j.jseaes.2017.04.003

Arne, D., Worley, B., Wilson, C., Chen, S. F., Foster, D., Luo, Z. L., … Dirks, P. (1997). Differential exhumation in response to episodic thrusting along the eastern margin of the Tibetan Plateau. *Tectonophysics*, *280*(3–4), 239–256. https://doi.org/10.1016/S0040-1951(97)00040-1

Beaumont, C., Jamieson, R. A., Nguyen, M. H., & Lee, B. (2001). Himalayan tectonics explained by extrusion of a low-viscosity channel coupled to focused surface denudation. *Nature*, *414*(6865), 738–742. https://doi.org/10.1038/414738a

Bureau of Geology and Mineral Resources of Sichuan Province (BGMRSP) (1991). *Regional Geology of Sichuan Province* (p. 730). Beijing: Geological Publishing House.

Bolle, O., Trindade, R. I. F., Bouchez, J. L., & Duchesne, J. C. (2002). Imaging downward magma transport in the Rogaland igneous complex (NW Norway). *Terra Nova*, *14*(2), 87–92. https://doi.org/10.1046/j.1365-3121.2002.00393.x

Bonvalot, S., Balmino, G., Briais, A., Kuhn, M., Peyrefitte, A., Vales, N., … Sarrailh, M. (2012). World gravity map. (1:50000000 map), BGI-CGMW-CNES-IRD, Paris.

Borradaile, G., & Henry, B. (1997). Tectonic applications of magnetic susceptibility and its anisotropy. *Earth-Science Reviews*, *42*(1–2), 49–93. https://doi.org/10.1016/S0012-8252(96)00044-X

Borradaile, G. J., & Jackson, M. (2004). Anisotropy of magnetic susceptibility (AMS): Magnetic petrofabrics of deformed rocks. *Geological Society, London, Special Publications*, *238*(1), 299–360. https://doi.org/10.1144/GSL.SP.2004.238.01.18

Borradaile, G. J., & Jackson, M. (2010). Structural geology, petrofabrics and magnetic fabrics (AMS, AARM, AIRM). *Journal of Structural Geology*, *32*, 1519–1551. https://doi.org/10.1016/j.jsg.2009.09.006

Bouchez, J. L. (2000). Anisotropie de susceptibilité magnétique et fabrique des granites. *Comptes Rendus de l'Académie des Sciences - Series IIA - Earth and Planetary Science*, *330*(1), 1–14. https://doi.org/10.1016/S1251-8050(00)00120-8

Bouchez, J. L., & Gleizes, G. (1995). Two-stage deformation of the Mount-Louis-Andorra granite pluton (Variscan Pyrenees) inferred from magnetic susceptibility anisotropy. *Journal of the Geological Society*, *152*(4), 669–679. https://doi.org/10.1144/gsjgs.152.4.0669

Bouchez, J. L., Hutton, D., & Stephens, W. E. (1997). *Granite is Never Isotropic: An Introduction to AMS Studies of Granitic Rocks. Granite: From Segregation of Melt to Emplacement Fabrics* (pp. 95–112). Paris: Springer Science & Business Media. https://doi.org/10.1007/978-94-017-1717-5_6

Burchfiel, B. C., Chen, Z., Liu, Y., & Royden, L. H. (1995). Tectonics of the Longmen Shan and adjacent regions, Central China. *International Geology Review*, *37*(8), 661–735. https://doi.org/10.1080/00206819509465424

Burchfiel, B. C., Royden, L. H., van der Hilst, R. D., Hager, B. H., Chen, Z., King, R. W., … Kirby, E. (2008). A geological and geophysical context for the Wenchuan earthquake of 12 May 2008, Sichuan, People's Republic of China. *Geological Society of America Bulletin Today*, *18*, 4–11. https://doi.org/10.1130/gsatg18a.1

Calassou, S. (1994). Etude tectonique d'une chaîne de décollement. A- Tectonique triasique et tertiaire de la chaîne de Songpan Garzê (Est Tibet). Thes, Diploma de Doctorat, Universite de Montpellier II.

Castonguay, S., Ruffet, G., & Tremblay, A. (2007). Dating polyphase deformation across low-grade metamorphic belts: An example based on $^{40}Ar/^{39}Ar$ muscovite age constraints from the southern Quebec Appalachians, Canada. *Geological Society of America Bulletin*, *119*, 978–992. https://doi.org/10.1130/b26046.1

Chen, J., Ma, R., Zhang, L., Li, X., He, X., & Hu, X. (2015). Zircon U-Pb dating and geochemical characters of diabase in the Shuimo area, northern section of the Longmen Shan. *Geology and Exploration*, *51*(1), 133–142.

Chen, S., Deng, Q., Zhao, X., Wilson, C. J. L., Dirks, P., Luo, Z., & Liu, S. (1994). Deformational characteristics, evolutionary history, and deformation mechanism of the middle Longmenshan thrust—Nappes and related tectonics. *Seismology and Geology*, *16*(4), 413–421.

Chen, S., & Wilson, C. J. K. (1996). Emplacement of the Longmen Shan Thrust—Nappe Belt along the eastern margin of the Tibetan Plateau. *Journal of Structural Geology*, *18*(4), 413–430. https://doi.org/10.1016/0191-8141(95)00096-V

Chen, S., Wilson, C. J. L., Luo, Z., & Deng, Q. (1994). The evolution of the western Sichuan Foreland Basin, southwestern China. *Journal of Asian Earth Sciences*, *10*(3–4), 159–168. https://doi.org/10.1016/0743-9547(94)90016-7

Chen, S., Wilson, C. J. L., & Worley, B. A. (1995). Tectonic transition from the Songpan-Garzê Fold Belt to the Sichuan Basin, south-western China. *Basin Research*, *7*(3), 235–253. https://doi.org/10.1111/j.1365-2117.1995.tb00108.x

Cook, K. L., Royden, L. H., Burchfiel, B. C., Lee, Y. H., & Tan, X. (2013). Constraints on Cenozoic tectonics in the southwestern Longmen Shan from low-temperature thermochronology. *Lithosphere*, *5*(4), 393–406. https://doi.org/10.1130/l263.1

Dirks, P., Wilson, C., Chen, S., Luo, Z., & Liu, S. (1994). Tectonic evolution of the NE margin of the Tibetan Plateau; evidence from the central Longmen Mountains, Sichuan Province, China. *Journal of Southeast Asian Earth Sciences*, *9*(1–2), 181–192. https://doi.org/10.1016/0743-9547(94)90074-4

Dunlop, D. J. (2002). Theory and application of the day plot (Mrs/Ms versus Hcr/Hc) 1. Theoretical curves and tests using titanomagnetite data. *Journal of Geophysical Research*, *107*(B3), 2056. https://doi.org/10.1029/2001JB000487

Enkelmann, E., Ratschbacher, L., Jonckheere, R., Nestler, R., Fleischer, M., Gloaguen, R., … Ma, Y.-S. (2006). Cenozoic exhumation and deformation of northeastern Tibet and the Qinling: Is Tibetan lower crustal flow diverging around the Sichuan Basin? *Geological Society of America Bulletin*, *118*, 651–671. https://doi.org/10.1130/b25805.1

Feng, S., Zhang, P., Liu, B., Wang, M., Zhu, S., Ran, Y., … Zheng, D. (2015). Deep crustal deformation of the Longmen Shan, eastern margin of the Tibetan Plateau, from seismic reflection survey and finite element modelling. *Journal of Geophysical Research: Solid Earth*, *121*, 767–787. https://doi.org/10.1002/2015JB012352

Ferré, E. C. (2002). Theoretical models of intermediate and inverse AMS fabrics. *Geophysical Research Letters*, *29*(7), 1127. https://doi.org/10.1029/2001GL014367

Godard, V., Pik, R., Lavé, J., Cattin, R., Tibari, B., de Sigoyer, J., … Zhu, J. (2009). Late Cenozoic evolution of the central Longmen Shan, eastern Tibet: Insight from (U-Th)/He thermochronometry. *Tectonics*, *28*, TC2009. https://doi.org/10.1029/2008TC002407

Grimmer, J. C., Glodny, J., Druppel, K., Greiling, R. O., & Kontny, A. (2015). Early- to mid-Silurian extrusion wedge tectonics in the central Scandinavian Caledonides. *Geology*, *43*(4), 347–350. https://doi.org/10.1130/g36433.1

Guineberteau, B., Bouchez, J. L., & Vigneresse, J. L. (1987). The Mortagne granite pluton (France) emplaced by pull-apart along a shear zone: Structural and gravimetric arguments and regional implication. *Geological Society of America Bulletin*, *99*(6), 763–770. https://doi.org/10.1130/0016-7606

Guo, X., Gao, R., Randy Keller, G., Xu, X., Wang, H., & Li, W. (2013). Imaging the crustal structure beneath the eastern Tibetan Plateau and implications for the uplift of the Longmen Shan range. *Earth and Planetary Science Letters*, *379*, 72–80. https://doi.org/10.1016/j.epsl.2013.08.005

Hargraves, R. B., Johnson, D., & Chan, C. Y. (1991). Distribution anisotropy: The cause of AMS in igneous rocks? *Geophysical Research Letters*, *18*(12), 2193–2196. https://doi.org/10.1029/91GL01777

Harrowfield, M. J., & Wilson, C. J. (2005). Indosinian deformation of the Songpan Garzê fold belt, northeast Tibetan Plateau. *Journal of Structural Geology*, *27*(1), 101–117. https://doi.org/10.1016/j.jsg.2004.06.010

Hartz, E. H., & Andresen, A. (1997). From collision to collapse: Complex strain permutations in the hinterland of the Scandinavian Caledonides. *Journal of Geophysical Research*, *102*(B11), 24,697–24,711. https://doi.org/10.1029/97JB02275

Hu, J., Meng, Q., Shi, Y., & Qu, H. (2005). SHRIMP U-Pb dating of zircons from granitoid bodies in the Songpan-Ganzi terrane and its implications. *Acta Petrologica Sinica*, *21*, 867–880.

Huang, M. H., Buick, I. S., Hou, L. W., Huang, M. H., & Hou, L. W. (2003). Tectonometamorphic evolution of the eastern Tibet Plateau: Evidence from the central Songpan-Garze orogenic belt, western China. *Journal of Petrology*, *44*(2), 255–278. https://doi.org/10.1093/petrology/44.2.255

Huang, M., Maas, R., Buick, I. S., & Williams, I. S. (2003). Crustal response to continental collisions between the Tibet, Indian, South China and North China blocks: Geochronological constraints from the Songpan-Garzê Orogenic Belt, western China. *Journal of Metamorphic Geology*, *21*(3), 223–240. https://doi.org/10.1046/j.1525-1314.2003.00438.x

Hubbard, J., & Shaw, J. H. (2009). Uplift of the Longmen Shan and Tibetan Plateau, and the 2008 Wenchuan (M = 7.9) earthquake. *Nature*, *458*(7235), 194–197. https://doi.org/10.1038/nature07837

Jelinek, V. (1981). Characterization of the magnetic fabric of rocks. *Tectonophysics*, *79*(3–4), T63–T67. https://doi.org/10.1016/0040-1951(81)90110-4

Jia, D., Wei, G., Chen, Z., Li, B., Zeng, Q., & Yang, G. (2006). Longmen Shan fold-thrust belt and its relation to the western Sichuan Basin in central China: New insights from hydrocarbon exploration. *AAPG Bulletin*, *90*, 1425–1447. https://doi.org/10.1306/03230605076

Johnston, S. M., Hartz, E. H., Brueckner, H. K., & Gehrels, G. E. (2010). U–Pb zircon geochronology and tectonostratigraphy of southern Liverpool Land, East Greenland: Implications for deformation in the overriding plates of continental collisions. *Earth and Planetary Science Letters*, *297*, 512–524. https://doi.org/10.1016/j.epsl.2010.07.003

Kirby, E., Reiners, P. W., Krol, M. A., Whipple, K. X., Hodges, K. V., Farley, K. A., … Chen, Z. (2002). Late Cenozoic evolution of the eastern margin of the Tibetan Plateau: Inferences from 40Ar/39Ar and (U–Th)/He thermochronology. *Tectonics*, *21*(1), 1–20. https://doi.org/10.1029/2000TC001246

Kruckenberg, S. C., Ferré, E. C., Teyssier, C., Vanderhaeghe, O., Whitney, D. L., Seaton, N. C. A., & Skord, J. A. (2010). Viscoplastic flow in migmatites deduced from fabric anisotropy: An example from the Naxos dome, Greece. *Journal of Geophysical Research*, *115*, B09401. https://doi.org/10.1029/2009JB007012

Li, Y., Jia, D., Shaw, J. H., Hubbard, J., Lin, A., Wang, M., … Wu, L. (2010). Structural interpretation of the coseismic faults of the Wenchuan earthquake: Three-dimensional modeling of the Longmen Shan fold-and-thrust belt. *Journal of Geophysical Research*, *115*, B04317. https://doi.org/10.1029/2009JB006824

Li, Y., Su, D., Zhou, R., Li, H., Densmore, A. L., Yan, L., & Yan, Z. (2013). Episodic orogeny deduced from coeval sedimentary sequences in the foreland basin and its implication for uplift process of Longmen Mountain, China. *Journal of Mountain Science*, *10*(1), 29–42. https://doi.org/10.1007/s11629-013-2238-z

Li, Z. (2009). Composition, structural characteristics and evolution of back-Longmenshan orogen (north section) in the northwest margin of Yangtze block, Doctoral thesis (211 pp.). Chang'an University.

Lin, W., Charles, N., Chen, Y., Chen, K., Faure, M., Wu, L., … Wang, Q. (2013). Late Mesozoic compressional to extensional tectonics in the Yiwulüshan massif, NE China and their bearing on the Yinshan–Yanshan orogenic belt: Part II: Anisotropy of magnetic susceptibility and gravity modeling. *Gondwana Research*, *23*(1), 78–94, https://doi.org/10.1016/j.gr.2012.02.012.

Long, X. (1991). Several questions of geochronic evolution in the mid-northeast segment of Longmenshan mountains. *Journal of Chengdu College of Geology*, *18*(1), 8–16.

Lu, R., He, D., John, S., Wu, J. E., Liu, B., & Chen, Y. (2014). Structural model of the central Longmen Shan thrusts using seismic reflection profiles: Implications for the sediments and deformations since the Mesozoic. *Tectonophysics*, *630*, 43–53. https://doi.org/10.1016/j.tecto.2014.05.003

Ma, Y., Wang, G., & Hu, X. (1996). Tectonic deformation of Pengguan complex. *Acta Geologica Sichuan*, *2*, 110–114.

Muxworthy, A., Heslop, D., & Williams, W. (2004). Influence of magnetostatic interactions on first-order-reversal-curve (FORC) diagrams: A micromagnetic approach. *Geophysical Journal International*, *158*, 888–897. https://doi.org/10.1111/j.1365-246X.2004.02358.x

Nédélec, A., & Bouchez, J. L. (2015). Genesis of hybrid granitoids: Mingling and mixing. In *Granites: Petrology, Structure, Geological Setting and Metallogeny* (pp. 58–72). Oxford University Press. https://doi.org/10.1093/acprof:oso

Parsons, A. J., Ferré, E. C., Law, R. D., Lloyd, G. E., Phillips, R. J., & Searle, M. P. (2016). Orogen-parallel deformation of the Himalayan midcrust: Insights from structural and magnetic fabric analyses of the Greater Himalayan Sequence, Annapurna-Dhaulagiri Himalaya, central Nepal. *Tectonics*, *35*, 2515–2537. https://doi.org/10.1002/2016TC004244

Parsons, A. J., Law, R. D., Lloyd, G. E., Phillips, R. J., & Searle, M. P. (2016). Thermo-kinematic evolution of the Annapurna-Dhaulagiri Himalaya, central Nepal: The composite orogenic system. *Geochemistry, Geophysics, Geosystems*, *17*(4), 1511–1539. https://doi.org/10.1002/2015GC006184

Paterson, S. R., Fowler, T. K., Schmidt, K. L., Yoshinobu, A. S., Yuan, E. S., & Miller, R. B. (1998). Interpreting magmatic fabric patterns in plutons. *Lithos*, *44*(1–2), 53–82. https://doi.org/10.1016/S0024-4937(98)00022-X

Paterson, S. R., Vernon, R. H., & Tobisch, O. T. (1989). A review of criteria for the identification of magmatic and tectonic foliations in granitoids. *Journal of Structural Geology*, *11*(3), 349–363. https://doi.org/10.1016/0191-8141(89)90074-6

Pinet, N., Tremblay, A., & Sosson, M. (1996). Extension versus shortening models for hinterland-directed motions in the southern Québec Appalachians. *Tectonophysics*, *267*(1–4), 239–256. https://doi.org/10.1016/S0040-1951(96)00096-0

Price, R. A. (1986). The southeastern Canadian Cordillera: Thrust faulting, tectonic wedging, and delamination of the lithosphere. *Journal of Structural Geology*, *8*(3–4), 239–254. https://doi.org/10.1016/0191-8141(86)90046-5

Rochette, P., Jackson, M., & Aubourg, C. (1992). Rock magnetism and the interpretation of anisotropy of magnetic susceptibility. *Reviews of Geophysics*, *30*(3), 209–226. https://doi.org/10.1029/92RG00733

Roger, F., Jolivet, M., Cattin, R., & Malavieille, J. (2011). Mesozoic-Cenozoic tectonothermal evolution of the eastern part of the Tibetan Plateau (Songpan-Garze, Longmen Shan area): Insights from thermochronological data and simple thermal modelling. *Geological Society of London, Special Publication*, *22*(5), 465–481. https://doi.org/10.1016/s1367-9120(03)00089-0

Roger, F., Malavieille, J., Leloup, P. H., Calassou, S., & Xu, Z. (2004). Timing of granite emplacement and cooling in the Songpan–Garzê Fold Belt (eastern Tibetan Plateau) with tectonic implications. *Journal of Asian Earth Sciences*, *22*(5), 465–481. https://doi.org/10.1016/s1367-9120(03)00089-0

Royden, L. H., Burchfiel, B. C., & van der Hilst, R. D. (2008). The geological evolution of the Tibetan Plateau. *Science*, *321*, 1054–1058. https://doi.org/10.1126/science.1155371

Schmid, S., Fügenschuh, B., Kissling, E., & Schuster, R. (2004). Tectonic map and overall architecture of the Alpine orogen. *Eclogae Geologicae Helvetiae*, *97*, 93–117. https://doi.org/10.1007/s00015-004-1113-x

Selverstone, J. (2005). Are the Alps collapsing? *Annual Review of Earth and Planetary Sciences*, *33*(1), 113–132. https://doi.org/10.1146/annurev.earth.33.092203.122535

Sen, K., Mukherjee, B. K., & Collins, A. S. (2014). Interplay of deformation and magmatism in the Pangong Transpression Zone, eastern Ladakh, India: Implications for remobilization of the trans-Himalayan magmatic arc and initiation of the Karakoram Fault. *Journal of Structural Geology*, *62*, 13–24. https://doi.org/10.1016/j.jsg.2014.01.009

Sigoyer, J., Vanderhaeghe, O., Duchêne, S., & Billerot, A. (2014). Generation and emplacement of Triassic granitoids within the Songpan Ganze accretionary-orogenic wedge in a context of slab retreat accommodated by tear faulting, eastern Tibetan Plateau, China. *Journal of Asian Earth Sciences*, *88*, 192–216. https://doi.org/10.1016/j.jseaes.2014.01.010

Stephenson, A. (1994). Distribution anisotropy: Two simple models for magnetic lineation and foliation. *Physics of the Earth and Planetary Interiors*, *82*(1), 49–53. https://doi.org/10.1016/0031-9201(94)90101-5

Talbot, J.-Y., Faure, M., Chen, Y., & Martelet, G. (2005). Pull-apart emplacement of the Margeride granitic complex (French Massif Central). Implications for the late evolution of the Variscan orogen. *Journal of Structural Geology*, *27*, 1610–1629. https://doi.org/10.1016/j.jsg.2005.05.008

Tapponnier, P., Peltzer, G., Dain, A. Y. L., Armijo, R., & Cobbold, P. (1982). Propagating extrusion tectonics in Asia: New insights from simple experiments with plasticine. *Geology*, *10*(12), 611–616. https://doi.org/10.1130/0091-7613

Tapponnier, P., Xu, Z., Roger, F., Meyer, B., Arnaud, N., Wittlinger, G., & Jingsui, Y. (2001). Oblique stepwise rise and growth of the Tibet Plateau. *Science*, *294*(5547), 1671–1677. https://doi.org/10.1126/science.105978

Tarling, D., & Hrouda, F. (1993). *Magnetic Anisotropy of Rocks*. London: Springer Science & Business Media.

Tavarnelli, E. (1999). Normal faults in thrust sheets: Pre-orogenic extension, post-orogenic extension, or both? *Journal of Structural Geology*, *21*(8–9), 1011–1018. https://doi.org/10.1016/S0191-8141(99)00034-6

Tian, Y., Kohn, B. P., Gleadow, A. J. W., & Hu, S. (2013). Constructing the Longmen Shan eastern Tibetan Plateau margin: Insights from low-temperature thermochronology. *Tectonics*, *32*, 576–592. https://doi.org/10.1002/tect.20043

Tian, Y., Kohn, B. P., Phillips, D., Hu, S., Gleadow, A. J., & Carter, A. (2016). Late Cretaceous–earliest Paleogene deformation in the Longmen Shan fold-and-thrust belt, eastern Tibetan Plateau margin: Pre-Cenozoic thickened crust? *Tectonics*, *35*, 2293–2312. https://doi.org/10.1002/2016TC004182

Turrillot, P., Faure, M., Martelet, G., Chen, Y., & Augier, R. (2011). Pluton-dyke relationships in a Variscan granitic complex from AMS and gravity modelling. Inception of the extensional tectonics in the South Armorican Domain (France). *Journal of Structural Geology*, *33*, 1681–1698. https://doi.org/10.1016/j.jsg.2011.08.004

Wallis, D., Parsons, A. J., Phillips, R. J., Searle, M. P., Ferré, E. C., & Ferre, E. C. (2014). Comment on "interplay of deformation and magmatism in the Pangong Transpressional Zone, Eastern Ladakh, India: Implications for remobilization of the trans-Himalayan magmatic arc and initiation of the Karakoram Fault" by K. Sen, BK Mukherjee and AS Collins, journal of structural geology 62 (2014) 13–24. *Journal of Structural Geology*, *65*, 117–119. https://doi.org/10.1016/j.jsg.2014.03.008

Wang, E., Kirby, E., Furlong, K. P., van Soest, M., Xu, G., Shi, X., … Hodges, K. V. (2012). Two-phase growth of high topography in eastern Tibet during the Cenozoic. *Nature Geoscience*, *5*, 640–645. https://doi.org/10.1038/ngeo1538

Wei, W., Chen, Y., Faure, M., Shi, Y., Martelet, G., Hou, Q., … Wang, Q. (2014). A multidisciplinary study on the emplacement mechanism of the Qingyang–Jiuhua massif in Southeast China and its tectonic bearings. Part I: Structural geology, AMS and paleomagnetism. *Journal of Asian Earth Sciences*, *86*, 76–93. https://doi.org/10.1016/j.jseaes.2013.06.003

Wei, W., Martelet, G., Le Breton, N., Shi, Y., Faure, M., Chen, Y., … Wang, Q. (2014). A multidisciplinary study of the emplacement mechanism of the Qingyang–Jiuhua massif in Southeast China and its tectonic bearings. Part II: Amphibole geobarometry and gravity modeling. *Journal of Asian Earth Sciences*, *86*, 94–105. https://doi.org/10.1016/j.jseaes.2013.09.021

White, A. P., & Hodges, K. V. (2002). Multistage extensional evolution of the central East Greenland Caledonides. *Tectonics*, *21*(5), 1048. https://doi.org/10.1029/2001TC001308

Worley, B., Wilson, C. J. L., Liu, S., & Luo, Z. (1995). Structural observations from the Wenchuan-Maowen metamorphic belt, Longmen Mountains, China. *Journal of Chengdu College of Geology*, *22*(01), 24–41.

Worley, B. A., & Wilson, C. J. (1996). Deformation partitioning and foliation reactivation during transpressional orogenesis, an example from the central Longmen Shan, China. *Journal of Structural Geology*, *18*(4), 395–411. https://doi.org/10.1016/0191-8141(95)00095-U

Xiao, L., Zhang, H., Clemens, J. D., Wang, Q. W., Kan, Z. Z., Wang, K. M., … Liu, X. M. (2007). Late Triassic granitoids of the eastern margin of the Tibetan Plateau: Geochronology, petrogenesis and implications for tectonic evolution. *Lithos*, *96*(3–4), 436–452. https://doi.org/10.1016/j.lithos.2006.11.011

Xu, Z., Hou, L., & Wang, Z. (1992). *Orogenic Process of the Songpan-Ganzé Orogenic Belt of China* (pp. 1–189). Beijing: Geological Publishing House.

Xu, Z., Ji, S., Li, H., Hou, L., Fu, X., & Cai, Z. (2008). Uplift of the Longmen Shan range and the Wenchuan earthquake. *Episodes*, *31*, 291–301.

Xu, Z., Li, H., Hou, L., Fu, X., Chen, W., Zeng, L., … Chen, F. (2007). Uplift of the Longmen-Jinping orogenic belt along the eastern margin of the Qinghai-Tibet Plateau: Large-scale detachment faulting and extrusion mechanism. *Geological Bulletin of China*, *26*, 1262–1276.

Yan, D., Zhou, M., Li, S., & Wei, G. (2011). Structural and geochronological constraints on the Mesozoic-Cenozoic tectonic evolution of the Longmen Shan thrust belt, eastern Tibetan Plateau. *Tectonics*, *30*, TC6005. https://doi.org/10.1029/2011TC002867

Yan, D., Zhou, M., Wei, G., Gao, J., Liu, S., Xu, P., & Shi, X. (2008). The Pengguan tectonic dome of Longmen Mountains, Sichuan Province: Mesozoic denudation of a Neoproterozoic magmatic arc-basin system. *Science in China Series D: Earth Sciences*, *51*, 1545–1559. https://doi.org/10.1007/s11430-008-0126-0

Yin, A., & Harrison, T. M. (2000). Geologic evolution of the Himalayan-Tibetan orogen. *Annual Review of Earth and Planetary Sciences*, *28*(1), 211–280. https://doi.org/10.1146/annurev.earth.28.1.211

Yuan, H., Zhang, Z., & Zhang, P. (1991). The uplift and cooling histories of Laojungou granite in the western margin of the central Longmen Mountain. *Journal of Chengdu College of Geology*, *18*(1), 17–22.

Zhang, H., Parrish, R., Zhang, L., Xu, W., Yuan, H., Gao, S., & Crowley, Q. G. (2007). A-type granite and adakitic magmatism association in Songpan–Garze fold belt, eastern Tibetan Plateau: Implication for lithospheric delamination. *Lithos*, *97*, 323–335. https://doi.org/10.1016/j.lithos.2007.01.002

Zhang, H., Zhang, L., Harris, N., Jin, L., & Yuan, H. (2006). U–Pb zircon ages, geochemical and isotopic compositions of granitoids in Songpan-Garze fold belt, eastern Tibetan Plateau: Constraints on petrogenesis and tectonic evolution of the basement. *Contributions to Mineralogy and Petrology*, *152*, 75–88. https://doi.org/10.1007/s00410-006-0095-2

Zhang, J., Gao, R., Zeng, L., Li, Q., Guan, Y., He, R., … Lu, Z. (2009). Relationship between characteristics of gravity and magnetic anomalies and the earthquakes in Longmenshan range and adjacent areas. *Chinese Journal of Geophysics*, *2*, 572–578.

Zhao, Y. (2007). Mesozoic granitoids in eastern Songpan-Garze: Geochemistry, petrogenesis and tectonic implications, thesis, Diploma of master, 111 pp, Graduate school Chinese Acad. Sci.

Zhou, M., Yan, D., Vasconcelos, P. M., Li, J., & Hu, R. (2008). Structural and geochronological constraints on the tectono-thermal evolution of the Danba domal terrane, eastern margin of the Tibetan Plateau. *Journal of Asian Earth Sciences*, *35*, 2781–2806. https://doi.org/10.1002/2016TC004210